Article

Immunity

A subset of Kupffer cells regulates metabolism through the expression of CD36

Graphical abstract

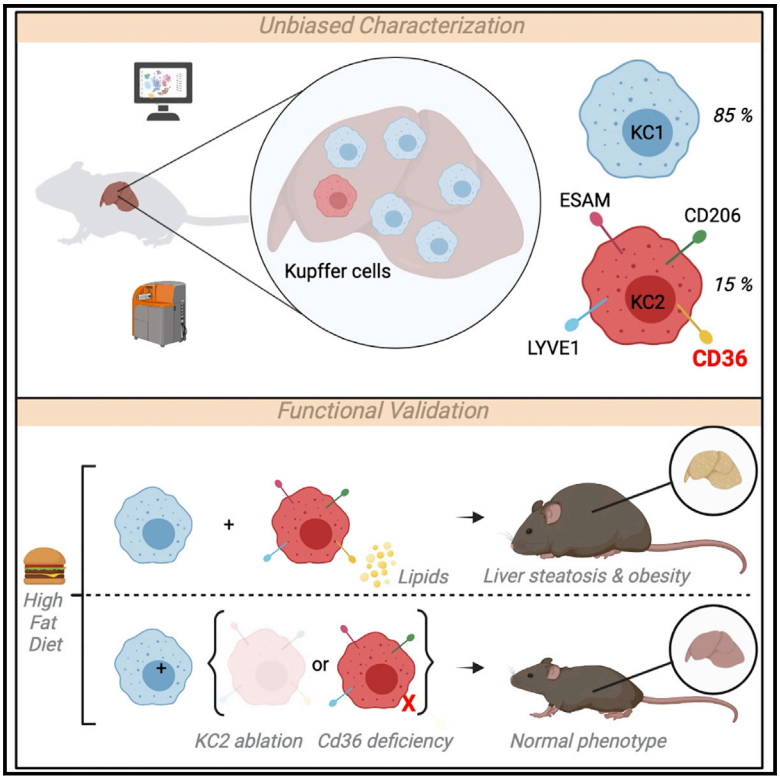

Highlights

- Unbiased high-throughput approaches reveal two subsets of murine Kupffer cells (KCs)
- CD206^{hi}ESAM^{+} KC2 exhibit a distinct metabolic signature
- Depletion of metabolically wired KC2 subset prevents diet-induced obesity
- CD36^{hi} KC2 regulate liver oxidative stress associated with obesity via CD36 expression

Authors

Camille Blériot, Emelie Barreby, Garett Dunsmore, ..., Matteo Iannacone, Myriam Aouadi, Florent Ginhoux

Correspondence

camille.bleriot@gustaveroussy.fr (C.B.), florent_ginhoux@immunol.a-star.edu.sg (F.G.)

In brief

Macrophage heterogeneity is well appreciated across tissues, but the diversity within the same tissue is often overlooked. Blériot et al. reveal the coexistence of two Kupffer cell subpopulations in murine liver with a minor CD206^{hi}CD36^{hi} one (KC2) endowed with metabolic functions, involved in regulating liver oxidative stress associated with obesity.

Blériot et al., 2021, Immunity *54*, 2101–2116
September 14, 2021
https://doi.org/10.1016/j.immuni.2021.08.006

CellPress

Immunity

CellPress

Article

A subset of Kupffer cells regulates metabolism through the expression of CD36

Camille Blériot,[1,2,*] Emelie Barreby,[3] Garett Dunsmore,[2] Raphaelle Ballaire,[4] Svetoslav Chakarov,[1,7] Xenia Ficht,[5] Giorgia De Simone,[5,6] Francesco Andreata,[5] Valeria Fumagalli,[5,6] Wei Guo,[7] Guochen Wan,[1] Gregoire Gessain,[1] Ahad Khalilnezhad,[1,8] Xiao Meng Zhang,[1] Nicholas Ang,[1] Ping Chen,[3] Cecilia Morgantini,[3] Valerio Azzimato,[3] Wan Ting Kong,[1] Zhaoyuan Liu,[7] Rhea Pai,[9] Josephine Lum,[1] Foo Shihui,[1] Ivy Low,[1] Connie Xu,[3] Benoit Malleret,[1,8] Muhammad Faris Mohd Kairi,[1] Akhila Balachander,[1] Olivier Cexus,[10] Anis Larbi,[1] Bernett Lee,[1] Evan W. Newell,[1] Lai Guan Ng,[1,8] Wint Wint Phoo,[11] Radoslaw M. Sobota,[11] Ankur Sharma,[9] Shanshan W. Howland,[1] Jinmiao Chen,[1] Marc Bajenoff,[12] Laurent Yvan-Charvet,[13] Nicolas Venteclef,[14] Matteo Iannacone,[5,6,15] Myriam Aouadi,[3] and Florent Ginhoux[1,7,8,16,17,*]

[1]Singapore Immunology Network (SIgN), Agency for Science, Technology and Research (A*STAR), Singapore 138648, Singapore
[2]Inserm U1015, Gustave Roussy, Villejuif 94800, France
[3]Center for Infectious Medicine, Department of Medicine, Karolinska Institute, Huddinge 14157, Sweden
[4]Inovarion, Paris 75005, France
[5]Division of Immunology, Transplantation and Infectious Diseases, IRCCS San Raffaele Scientific Institute, Milan 20132, Italy
[6]Vita-Salute San Raffaele University, Milan 20132, Italy
[7]Shanghai Institute of Immunology, Shanghai Jiao Tong University School of Medicine, Shanghai 200025, China
[8]Department of Microbiology and Immunology, Immunology Translational Research Program, Yong Loo Lin School of Medicine, Immunology Program, Life Sciences Institute, National University of Singapore, Singapore 117543, Singapore
[9]Genome Institute of Singapore, A*STAR, Singapore 138672, Singapore
[10]Biosciences and Medicine, Faculty of Health and Medical Sciences, University of Surrey, Guildford GU2 7XH, United Kingdom
[11]Functional Proteomics Laboratory, SingMass National Laboratory, Institute of Molecular and Cell Biology, Agency for Science, Technology and Research (A*STAR), Singapore 138673, Singapore
[12]Aix Marseille University, CNRS, INSERM, CIML, Marseille 13288, France
[13]UMR INSERM U1065/UNS, C3M, Nice 06204, France
[14]Centre de Recherche des Cordeliers, INSERM, Université de Paris, Sorbonne Université, IMMEDIAB Laboratory, Paris 75006, France
[15]Experimental Imaging Centre, IRCCS San Raffaele Scientific Institute, Milan 20132, Italy
[16]Translational Immunology Institute, SingHealth Duke-NUS Academic Medical Centre, Singapore 169856, Singapore
[17]Lead contact
*Correspondence: camille.bleriot@gustaveroussy.fr (C.B.), florent_ginhoux@immunol.a-star.edu.sg (F.G.)
https://doi.org/10.1016/j.immuni.2021.08.006

SUMMARY

Tissue macrophages are immune cells whose phenotypes and functions are dictated by origin and niches. However, tissues are complex environments, and macrophage heterogeneity within the same organ has been overlooked so far. Here, we used high-dimensional approaches to characterize macrophage populations in the murine liver. We identified two distinct populations among embryonically derived Kupffer cells (KCs) sharing a core signature while differentially expressing numerous genes and proteins: a major CD206^{lo}ESAM^{-} population (KC1) and a minor CD206^{hi}ESAM^{+} population (KC2). KC2 expressed genes involved in metabolic processes, including fatty acid metabolism both in steady-state and in diet-induced obesity and hepatic steatosis. Functional characterization by depletion of KC2 or targeted silencing of the fatty acid transporter *Cd36* highlighted a crucial contribution of KC2 in the liver oxidative stress associated with obesity. In summary, our study reveals that KCs are more heterogeneous than anticipated, notably describing a subpopulation wired with metabolic functions.

INTRODUCTION

Resident tissue macrophages (RTMs) are a diverse population of immune cells characterized by tissue-specific phenotypes and exhibiting a wide range of functions within their tissue of residence (Blériot et al., 2020a). The liver harbors a population of RTMs called Kupffer cells (KCs) lining liver sinusoids, specialized in detoxifying the blood traveling from the gut to the liver via the portal vein, which might contain microbionts, harmful enteropathogens or toxic by-products of digestion. Thus, KCs can break down old or damaged red blood cells; engulf incoming threats; and play a central role during inflammation, notably in the development of liver pathologies such as viral hepatitis, fibrosis, hepatocellular carcinomas, alcohol-related disorders,

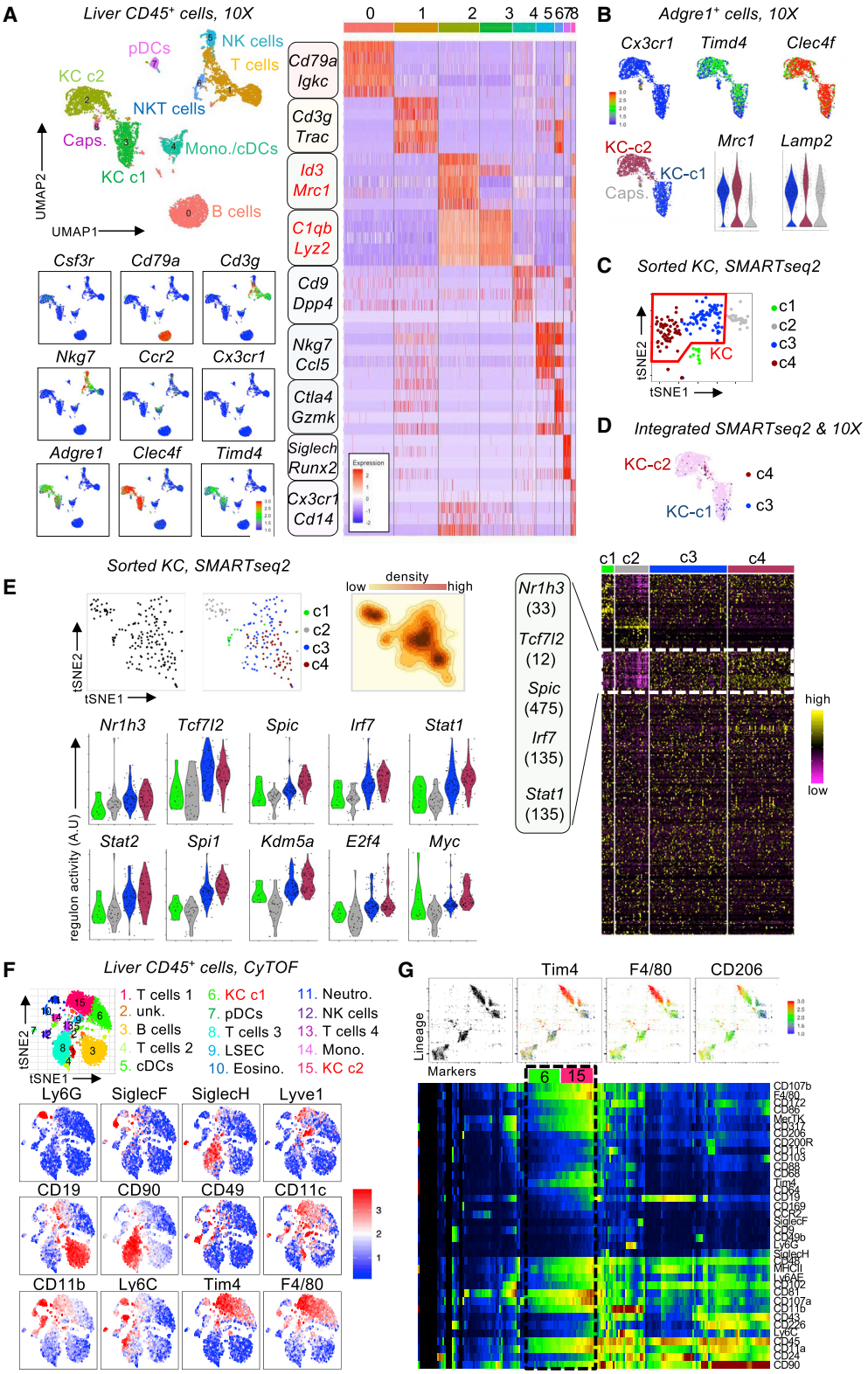

Figure 1. Unbiased approaches reveal KC heterogeneity

(A) CD45^{+} Tomato^{-} liver cells were extracted from healthy *Ms4a3*^{cre} x *Rosa*^{Tomato} mice, and libraries of mRNA were generated and sequenced using the chromium technology. Seurat analysis was conducted defining nine clusters with distinct patterns of gene expression. Each dot corresponds to a single cell, colored

(legend continued on next page)

or non-alcoholic steatohepatitis (NASH)/fatty liver disease (NAFLD) (Krenkel and Tacke, 2017). However, even if the involvement of KCs in these pathologies is undisputable, their precise modes of action remain largely unknown.

KCs derive from fetal liver monocytic precursors (Hashimoto et al., 2013; Hoeffel et al., 2015; Schulz et al., 2012; Yona et al., 2013), which acquire their identity early during embryonic development (Mass et al., 2016) and maintain themselves throughout life. Although early post-natal circulating monocytes contribute a minor fraction of KCs shortly after birth (Scott et al., 2016), KC renewal is almost completely independent of bone-marrow-derived cells in the steady state. However, under inflammatory conditions or when native embryonic KCs are depleted, monocyte-derived macrophages can replace dying embryonic KCs (Blériot et al., 2015; Scott et al., 2016). Moreover, alongside KCs, other minor populations of ontogenically and functionally unrelated macrophages—including capsular macrophages, or even peritoneal macrophages recruited after injury—reside in the liver (Blériot and Ginhoux, 2019; Sierro et al., 2017; Wang and Kubes, 2016). This results in a mosaic of hepatic macrophage populations that are heterogeneous in origin, phenotype, and functions, among which KCs are by far the most abundant.

Within the murine KC population, the existence of distinct subsets at steady state has been proposed in various studies (Beattie et al., 2016; David et al., 2016; Han et al., 2017; Klein et al., 2007), but their conclusions have proven difficult to distinguish between embryonic KCs and monocyte-derived macrophages. Whether these distinct populations play different roles in the pathophysiology of liver diseases also remains elusive. In human studies, while recent single-cell transcriptomic studies suggest the existence of two major subsets of liver macrophages, the functions of these distinct subsets also remain elusive (Aizarani et al., 2019; MacParland et al., 2018; Ramachandran et al., 2019). Here, we aimed at clarifying KC heterogeneity by combining single-cell transcriptomics to specific monocyte fate-mapping models and functional validation. We revealed the existence of two distinct KC populations in the steady-state murine liver: a major population of CD206^{lo} ESAM^{-} that we termed KC1 and a minor population of CD206^{hi} ESAM^{+} termed KC2. We confirmed the common embryonic origin of these populations and their independence from inflammatory monocytes and Tim4^{-} capsular macrophages. Functionally, we found that KC1 and KC2 have specific transcriptomic and proteomic signatures, and CD206^{hi} ESAM^{+} KC2 are involved in the regulation of liver metabolism in a murine model of obesity via their high expression of the fatty acid transporter CD36.

RESULTS

Unbiased approaches reveal KC transcriptomic heterogeneity

To assess the KC heterogeneity in an unbiased manner, we first employed single-cell RNA sequencing (RNA-seq) technology. We purified liver CD45^{+} leukocytes from steady-state murine liver and profiled thousands of individual cells by using the chromium single-cell gene expression technology (10X). A Seurat analysis (Butler et al., 2018) of this dataset with a uniform manifold approximation and projection (UMAP) dimension-reduction analysis (Becht et al., 2018) and an automatic clustering identified 9 main clusters (#0 to #8) in the CD45^{+} cell population (Figure 1A). These clusters were manually annotated by using canonical population markers: #0 represents B cells, #1 T cells, #4 monocytes and conventional dendritic cells (cDCs), #5 NK cells, #6 NKT cells, #7 plasmacytoid dendritic cells (pDCs), and #8 capsular macrophages. Concerning clusters #2 and #3, these cells co-expressed many genes being classically highly expressed by KCs such as *Adgre1* (encoding F4/80), *Timd4*, *Csf1r*, and *Clec4f* (Figure 1A). When focusing on total *Adgre1*$^{+}$ cells, a population that can be considered as liver macrophages, we identified a sub-cluster of *Cx3cr1*$^{+}$ *Timd4*$^{-}$*Clec4f*$^{-}$ cells corresponding to capsular macrophages (Sierro et al., 2017) and two clusters of *Cx3cr1*$^{-}$*Timd4*$^{+}$*Clec4f*$^{+}$ KCs expressing differentially genes such as *Mrc1* (CD206) and *Lamp2* (CD107b) (Figure 1B). In addition, using the high-resolution SMARTseq2 platform (Picelli et al., 2013), we have observed that sorted liver CD64^{+}F4/80^{+} cells could be split into four clusters (Figure 1C) (De Simone et al., 2021). From these clusters, only the two main ones, c3 and c4, harbored the canonical KC signature, while c1 and c2 displayed unrelated signatures, arguing from a contamination during cell sorting (Figure S1A). Then, by integrating the low-resolution 10X data generated on thousands of cells with the deeper but number-restricted SMARTseq2 data, we validated the presence of two clusters of KCs observed with two different single-cell RNA-seq technologies (Figure 1D). We then used the Scenic analytical pipeline (Aibar et al., 2017) to reveal regulatory networks in the most sensitive SMARTseq2 single-cell RNA-seq dataset. This confirmed that the full KC population harboring a pattern of regulon activity consistent with liver macrophages—with a high expression of canonical KC transcription factors such as *Nr1h3* (liver X receptor alpha) and *Spic* (Mass

according to the clusters identified. Expression of a few representative genes is overlaid to define each cluster, and a heatmap of the most highly differentially expressed genes (DEGs) in the different clusters is displayed.

(B) Zoom on the *Adgre1*$^{+}$ macrophage population showing the *Cx3cr1*$^{+}$ capsular macrophages and the two clusters of *Timd4*$^{+}$ *Clec4f*$^{+}$ KCs. Violin plots show expression of selected genes in the two KC clusters.

(C) t-Distributed stochastic neighbor embedding (tSNE) projection of sorted CD45^{+} CD64^{+} F4/80^{+} liver cells sequenced according to SMARTseq2 protocol (De Simone et al., 2021). Each dot corresponds to a single cell, colored according to the clusters identified. KC clusters correspond to c3 and c4.

(D) Integration of SMARTseq2 (probes) and chromium (reference) datasets focused on *Clec4f*$^{+}$ KCs for validation of the clustering.

(E) Scenic analysis of the high-resolution SMARTseq2 dataset with the overlay of the four clusters identified in the Seurat analysis. Two stable states within the macrophage population corresponding to Seurat c3 and c4 are visible. The number of genes included in each regulon is provided in parentheses.

(F) Dot plot representation of the expression of the indicated markers projected onto a tSNE analysis showing the different clusters in live liver CD45^{+} singlets analyzed with a 37-marker extended CyTOF panel. The unsupervised analysis was done with the Phenograph algorithm and revealed 15 clusters, manually assigned as indicated populations thanks to lineage markers.

(G) Analysis with the OneSENSE algorithm of live liver CD45^{+} singlets. F4/80^{+} Tim4^{+} KC cells are shown within a dashed black frame.

See also Figure S1.

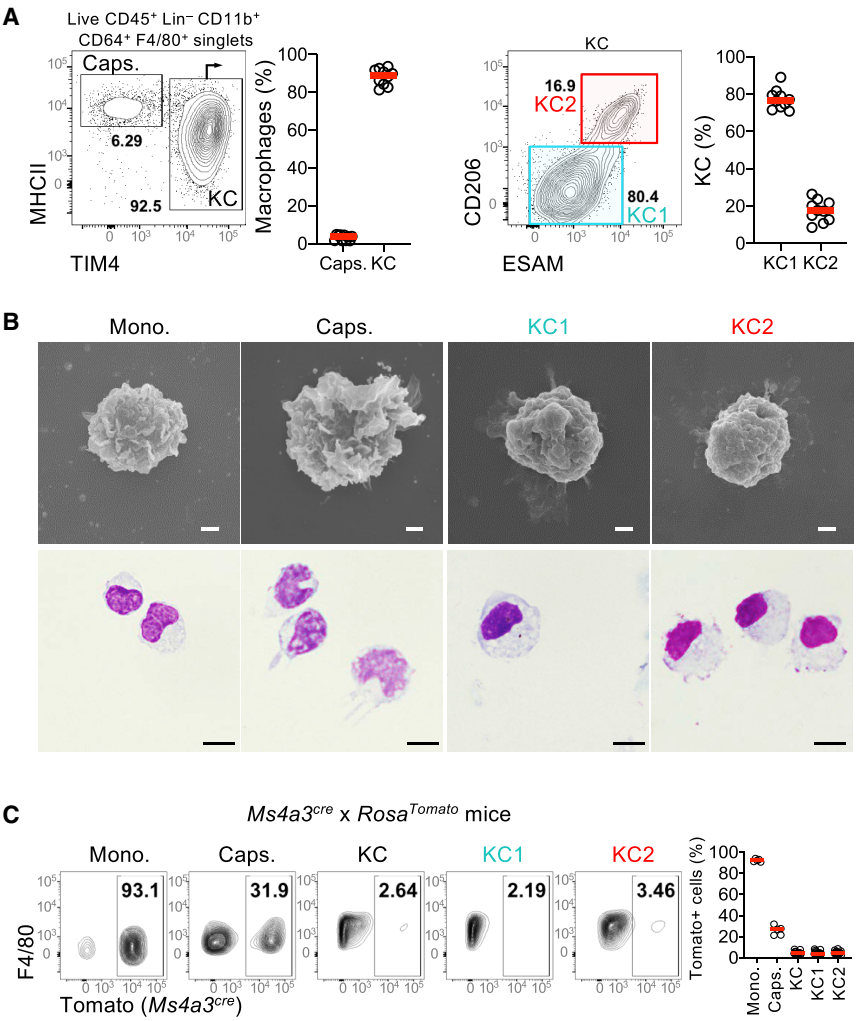

Figure 2. KCs can be divided into two subpopulations sharing a common origin

(A) Flow cytometry plots showing Tim4^{hi} KCs and MHCII^{hi} capsular macrophages among total macrophages (left) and CD206^{lo}ESAM^{-} KC1 and CD206^{hi}ESAM^{+} KC2 among KCs (right). For the quantification, each dot represents an individual, and the median is indicated by a red line.

(B) Scanning electron and optical (cytospin) microscopy images of flow cytometry sorted liver KC1, KC2, capsular macrophages, and monocytes. Scale bars, 1 μm.

(C) Flow cytometric measurement of the frequency of Tomato expression in indicated populations in 8-week-old *Ms4a3^{cre}* x *Rosa^{Tomato}* mice. Each dot represents an individual, and the median is indicated by a red line.

See also Figure S2.

et al., 2016; Scott et al., 2018)—could be split into two different states (Figure 1E). Moreover, each cluster of KCs displayed a specific regulon activity profile, (e.g., with *Runx3* being more active in c3 and *Klf6* more active in c4; Figure S1B).

Our unbiased single-cell RNA-seq approaches revealed two distinct subsets of KCs present at steady state. To validate these findings at the protein level, we used the mass cytometry technology to monitor the expression of an extended panel of common myeloid markers and putative markers identified by the unbiased single-cell transcriptomic approach such as CD206 and CD107b (Figures 1F and 1G). By integrating the expression of these markers in live CD45^{+} cells from steady-state murine liver, we identified the major immune cell subsets present in the liver: CD19^{+} B cells (#3), CD90^{+} T cells (#1, #4, #8, and #13), CD49b^{+} NK cells (#12), SiglecH^{+}BST2^{+} pDCs (#7), Ly6C^{+} monocytes (#14), CD11c^{+} cDCs (#5), SiglecF^{+} eosinophils (#10), Ly6G^{+} neutrophils (#11), and a large population of F4/80^{+}Tim4^{+} KCs comprising two clusters (#6 and #15) (Figures 1F and S1C). Focusing on this KC population, a One-SENSE (one-dimensional soli-expression by nonlinear stochastic embedding) analysis allowing the manual definition of lineage and marker dimensions (Cheng et al., 2016) revealed some markers differentially expressed by the two clusters within this population: notably, CD206 and CD107b, but also CD81, CD107a, and Lyve1 (Figure 1G). Therefore, by combining unbiased transcriptomic and proteomic approaches, we uncovered that KCs can be subdivided in CD206^{lo} CD107b^{-} (=KC1) and CD206^{hi} CD107b^{+} (=KC2) populations.

KCs can be divided into two subpopulations sharing a common embryonic origin

Based on this unsupervised approach, we designed a panel of markers for use in conventional flow cytometry to analyze the KC population. KCs are classically defined as CD45^{+}CD64^{+}F4/80^{+}TIM4^{+} Clec4F^{+} cells with low expression of CD11b and Ly6C (Figure S2A). We used CD206 and CD107b to identify and sort KC1 and KC2 and generate transcriptomic signatures of these two populations (Figure S2B). Among the top differentially expressed genes (DEGs) was *Esam*, a previously reported marker for splenic dendritic cells (Lewis et al., 2011). Therefore, we retained CD206 and ESAM as two reliable markers and used them later to define CD206^{lo} ESAM^{-} KC1 and CD206^{hi} ESAM^{+} KC2 by conventional flow cytometry (Figure 2A). We also measured expression of other markers highlighted as overexpressed by KC2 with high-throughput approaches, including CD63, CD81, CD107a, and Lyve1 on the two populations (Figure S2C). All these markers were expressed by KC2, and we could not identify any specific markers of KC1. However, KC1 and KC2 could be clearly distinguished either by manual gating based on CD206 and ESAM expression or by using algorithm-based dimension reduction (Figure S2D). Sorted KC1 and KC2 had comparable morphology and were indistinguishable by cytospin and electronic microscopy (Figures 2B and S2E).

We and others have shown that KCs derive from fetal liver monocytes with a minimal contribution of bone marrow monocytes to maintain the adult KC population (Hashimoto et al., 2013; Hoeffel et al., 2015; Schulz et al., 2012; Yona et al.,

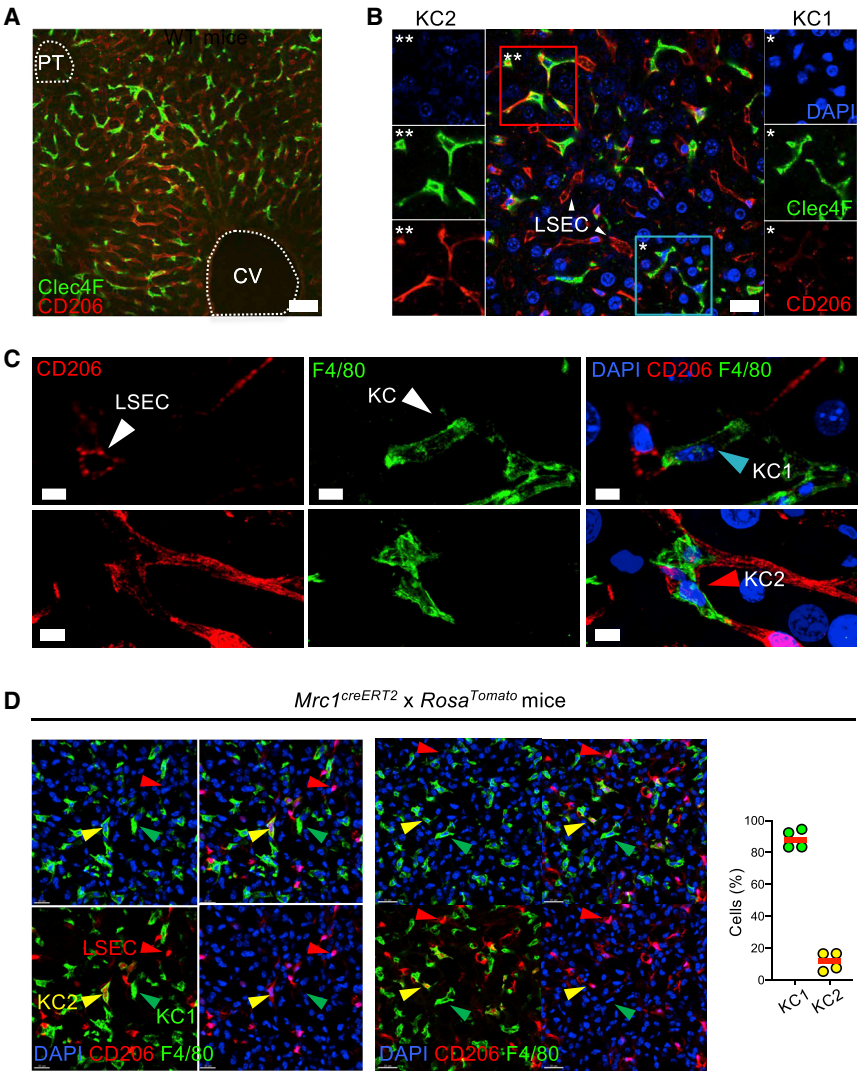

Figure 3. KC1 and KC2 have overlapping distribution patterns in the liver

(A and B) Low magnification (A) and high magnification (B) of immunofluorescence microscopy images of liver vibratome sections from WT C57BL/6 mice. Sections are labeled for Clec4F and CD206 and stained with DAPI. Scale bars, 20 μm (A) and 10 μm (B).

(C) Single *Z*-slices of fluorescent micrographs of single channels (CD206, red; F4/80, green) and merged images including DAPI [blue]) depicting examples of KC1 and KC2 after *in vivo* CD206 labeling. Scale bars, 5 μm.

(D) Immunofluorescence microscopy images of liver sections from $Mrc1^{creERT2}$ x $Rosa^{Tomato}$ mice treated with a single injection of tamoxifen 24 h before analysis. Sections are labeled for F4/80 and stained with DAPI. Scale bars, 20 μm. Quantification of $F4/80^{+}CD206^{lo}$ (KC1) and $F4/80^{+}CD206^{hi}$ (KC2) cells on independent fields is displayed.

See also Figure S3.

2013). But several reports have shown that monocyte-derived cells could acquire KC identity in non-homeostatic conditions (Beattie et al., 2016; Bonnardel et al., 2019; Sakai et al., 2019; Scott et al., 2016). Thus, to clarify the origin of the two subpopulations and accurately categorize them as bona fide KCs, we first checked when heterogeneity within the KC population emerged and analyzed the presence of KC1 and KC2 from birth to adulthood. While the ratio of monocytes to macrophages was dynamic during the first postnatal weeks, the ratio between KC1 and KC2 populations was very stable, being already established at birth, suggesting that they both arise from prenatal precursors (Figure S2F), even if we could not formally exclude that each subpopulation emerged during distinct waves in embryogenesis. We then used our monocyte fate-mapping $Ms4a3^{cre}$ x $Rosa^{Tomato}$ mouse model (Liu et al., 2019) to assess any possible monocytic contribution. As expected, monocytes and monocyte-derived capsular macrophages were highly tagged in adult mice, whereas KC1 and KC2 exhibited equal and very low tagging (Figure 2C). In addition, high and comparable reporter expression was observed in KC1 and KC2 in $Csf1r^{GFP}$ mice, confirming the macrophage nature of both subpopulations (Figure S2G).

Similar observations could be made by analyzing the $S100a4^{cre}$ x $Rosa^{YFP}$ hematopoietic stem cell (HSC) fate-mapping mouse model (Hashimoto et al., 2013; Hoeffel et al., 2015), which displayed low and similar tagging for KC1 and KC2, suggestive of their independence from the fully labeled adult monocyte contribution (Figure S2H). We have also confirmed this by analyzing CD45.1/CD45.2 parabiotic mice in which the non-host chimerism was very low after 3 months of shared systemic circulation in both KC1 and KC2, in contrast to monocyte-derived capsular macrophages (Figure S2I), as previously shown (Sierro et al., 2017). Taken together, these results show that both KC subsets are bona fide embryonically derived KCs and, therefore, do not represent ontogenically distinct populations but rather two different states of KCs.

KC1 and KC2 have overlapping distribution patterns *in situ*

To assess a potential differential sublocalization of the two subsets in the liver, we first checked their accessibility to an intravenously injected anti-CD45 antibody. KC1 and KC2 were labeled with a comparable efficiency, confirming their sinusoidal localization (Figure S3A). We then used two-photon microscopy to look at these cells *in situ* coupled with immunofluorescence microscopy of liver sections from wild-type (WT) mice for more detailed analysis. $Clec4F^{+}$ KCs were easily distinguished from the $Clec4F^{-}$ $CD206^{+}$ liver sinusoidal endothelial cells (LSECs), and KC2 were detected as $Clec4F^{+}$ or $F4/80^{+}$ KCs also expressing CD206 (Figures 3A–3C). To fully validate this, we generated $Mrc1^{creERT2}$ mice (Figure S3B) and bred them with $Rosa^{Tomato}$ mice in order to establish a model in which we can track cells expressing CD206 after tamoxifen induction. By immunostaining, we observed that around 15% of KCs were tagged with Tomato

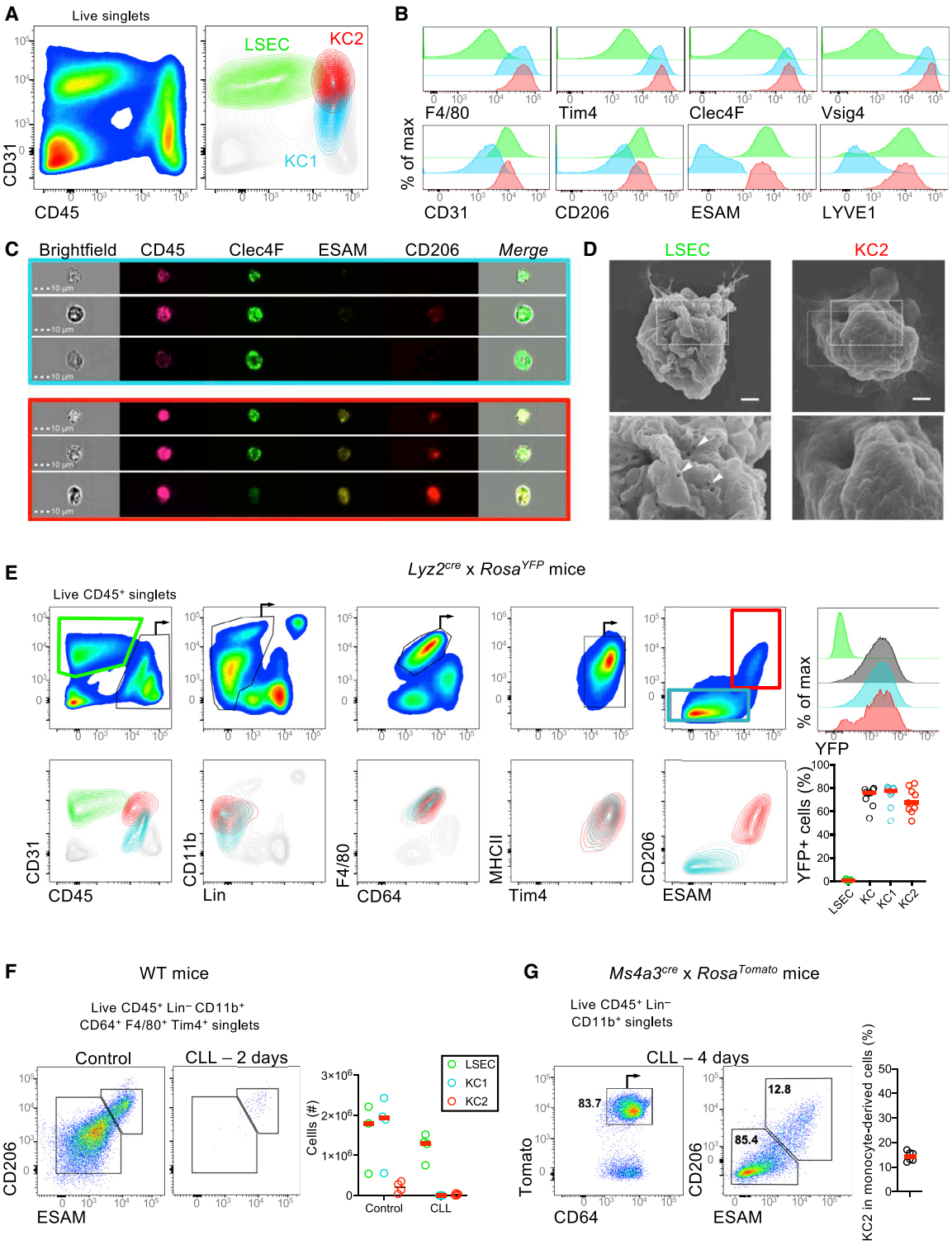

Figure 4. KC2 express endothelial markers but are distinct from LSECs

(A) Flow cytometry plots of the total liver onto which CD45$^-$ CD31$^+$ LSEC, CD45$^+$ Lin$^-$ F4/80$^+$ CD64$^+$ Tim4$^+$ ESAM$^-$CD206^{lo} KC1 and CD45$^+$ Lin$^-$ F4/80$^+$ CD64$^+$ Tim4$^+$ ESAM$^+$CD206^{hi} KC2 are projected.

(B) Flow cytometry profiles of the intensity of expression of indicated markers on the three populations.

(C) Imaging cytometry (image stream) analysis of liver cells. KC1 (blue) and KC2 (red) are shown.

(D) Scanning electron microscopy images of sorted liver LSECs and KC2. Scale bars, 1 μm. Fenestrae indicated by white arrows are shown in the magnified image.

(legend continued on next page)

in these mice, in accordance with the proportions observed by using the CD206 marker in conventional flow cytometry analysis (Figure 3D). We also measured the distance between F4/80^{+}CD206^{lo} KC1 and F4/80^{+}CD206^{hi} KC2 and their closest portal triad to assess whether hepatic metabolic zonation (Gebhardt, 1992; Jungermann and Saase, 1978) influenced KC1 and KC2 distribution. No significant differences were observed concerning the zonation of the two populations (Figure S3C). Taken together, these observations suggest that KC1 and KC2 have overlapping distribution patterns in the liver.

KC2 express LSEC-associated markers but are distinct from LSEC

Being macrophages, KC1 and KC2 express canonical macrophage markers such as F4/80, Tim4, Clec4F, and Vsig4. But KC2 also displayed markers known to be expressed by LSECs such as CD206, CD31, ESAM, and even Lyve1 that we have recently identified as a broad macrophage marker (Figures 4A and 4B) (Chakarov et al., 2019; Lim et al., 2018). To understand such expression patterns and exclude the possibility that their detection arose from phagocytosis of LSECs by KCs, we performed an image stream analysis coupling flow cytometry with microscopy, allowing the imaging of individual cells. We observed that ESAM and CD206 labeling was uniformly distributed across KC2 cells, arguing for surface expression of these markers (Figure 4C). Furthermore, LSECs have fenestrae on their surface, which were absent on KC2 cells (Figure 4D). Moreover, we analyzed *Lyz2^{cre} x Rosa^{YFP}* mice in which cells expressing the canonical myeloid gene *Lyz2* are tagged and observed that KC1 and KC2 were both highly labeled while LSECs were not tagged (Figure 4E). We also confirmed the macrophage nature of KC1 and KC2 by using the Rhapsody technology, which allows rapid parallel sequencing of 400 markers in thousands of single cells (Mair et al., 2020). Comparing this lower-resolution single-cell transcriptomic profile of sorted KC1 and KC2 to the whole liver leukocyte population, we found that both KC1 and KC2 clearly clustered in the macrophage population, further confirming their macrophage identity (Figure S4A). At the functional level, we used the clodronate liposome (CLL) approach (van Rooijen and Hendrikx, 2010) to test the phagocytic capacity of both populations: upon liposome injection, KC1 and KC2, but not LSECs, were similarly depleted, indicating comparable phagocytic activity (Figure 4F). In addition, KC depletion is known to induce a recruitment of monocytes that quickly acquire KC-like phenotypes even if few key KC genes such as *Timd4* are not re-expressed before several weeks (Scott et al., 2016). When CLL-mediated depletion was performed in *Ms4a3^{cre} x Rosa^{Tomato}* mice, we observed that CD64^{+}Tomato^{+}Tim4^{-} monocyte-derived macrophages quickly gave rise to both CD206^{lo} ESAM^{-} KC1-like and CD206^{hi} ESAM^{+} KC2-like populations in a ratio comparable to steady state (Figure 4G). This underlined the fact that recruited naive adult monocytes have the capacity to acquire both KC1- and KC2-like profiles and suggests that both KC1 and KC2 identities are strongly dictated by the liver microenvironment.

KC1 and KC2 exhibit distinct gene and protein expression signatures

We then sorted CD206^{lo} ESAM^{-} KC1 and CD206^{hi} ESAM^{+} KC2 to perform a deeper transcriptomic analysis using the SMART-seq2 protocol for bulk RNA-seq to better understand their functions. At this high resolution, the two populations were clearly separated from each other (Figures 5A–5C) and are distinct from sorted CD45^{-}CD31^{+} LSECs (Figures S4B and S4C). KC1 and KC2 expressed similarly canonical macrophage genes including *Clec4f*, *Lyz2*, *Vsig4*, *Csf1r*, and *Adgre1* (F4/80) (Figures S4D and S4E). In addition to this macrophage signature, as we found before, KC2 highly expressed numerous LSEC-associated genes—notably, *Mrc1*, *Pecam1* (CD31), *Esam*, *Kdr*, and *Lyve1.*

To confirm that these LSEC-associated genes were indeed expressed by KC2 and were not detected due to phagocytosis of LSECs, we assessed the actively transcribed RNA (translatome) of the two populations using the RiboTag strategy (Haimon et al., 2018; Sanz et al., 2009). We generated *Lyz2^{cre}* x *Rpl22^{HA}* mice in which we could purify the ribosomes from both KC1 and KC2 and sequenced the RNA associated with them. Using this method, even though the quantity of initial material and, accordingly, the global detected expression dropped, the dichotomy between KC1 and KC2 remained, including KC2 expression of the LSEC-associated genes *Mrc1*, *Esam*, and *Lyve1* (Figures 5D–5F). At the protein level, we also measured expression of around 4,500 proteins in sorted KC1 and KC2 by mass spectrometry and found comparable differentially expressed proteins (DEPs)—notably, ESAM and CD31—that were more abundant in KC2 (Figures 5G–5I). Finally, we integrated the transcriptome, translatome, and proteome data to generate robust KC1 and KC2 pan-omics identities (Figures 5J and S5A): while the core KC program was conserved across both populations (Figure S5B), pathway analysis identified a stronger immune signature for KC1, whereas cell adhesion and genes related to metabolic pathways—notably, *Cd36*—were upregulated in KC2 (Figures 5K and S5C–S5E).

KC2 exhibit metabolic functions

We further explored the significance of this pan-omics pronounced metabolic signature highlighted in the KC2 population. As we observed an upregulation of genes involved in carbohydrate and lipid metabolisms in KC2, we chose to use a model of high-fat diet (HFD) feeding, which induces obesity and its related metabolic disorders, including glucose intolerance and liver steatosis in mice (Figure 6A) (Jaitin et al., 2019; Wang and Liao, 2012). We noticed an increase in the relative frequency of

(E) Flow cytometric measurement of the frequency of YFP expression in indicated populations in 8-week-old *Lyz2^{cre}* x *Rosa^{YFP}* mice. KC1 (blue) and KC2 (red) are overlaid at each step of the gating strategy. Each dot represents an individual, and the median is indicated by a red line.
(F) Flow cytometric measurement of the frequency of LSEC, KC1, and KC2 populations in C57BL/6 mice after clodronate liposome (CLL)-mediated KC depletion. Each dot represents an individual, and the median is indicated by a red line.
(G) Flow cytometric measurement of the frequency of KC1 and KC2 populations in *Ms4a3^{cre} x Rosa^{Tomato}* mice after CLL-mediated KC depletion. Each dot represents an individual, and the median is indicated by a red line.
See also Figure S4.

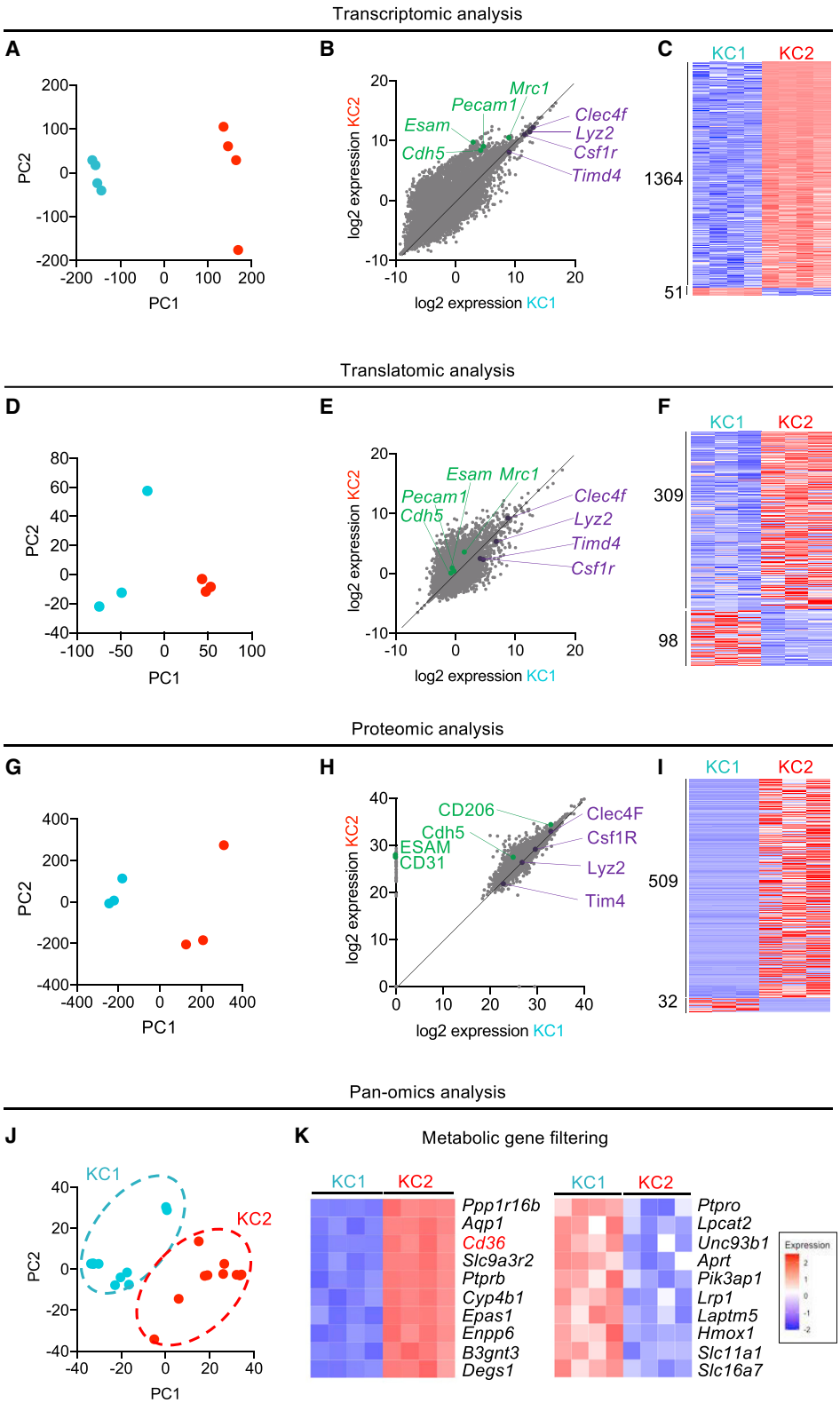

Figure 5. KC1 and KC2 exhibit distinct gene and protein expression signatures

(A) Principal-component analysis of the transcriptomes from bulk RNA-seq of sorted liver KC1 and KC2.

(B) Dot plot representation of the expression of genes expressed by KC1 and KC2. Genes known to be highly expressed in macrophages are highlighted in purple, and those described to be predominantly expressed in LSECs are in green.

(legend continued on next page)

the KC2 population as compared to mice fed a normal diet (Figure 6B). As reported previously (Jaitin et al., 2019; Morgantini et al., 2019), we did not notice any significant monocyte recruitment into the livers of our monocyte fate-mapper *Ms4a3*^{cre} x *Rosa*^{Tomato} mice in the 9 first weeks of HFD (Figure S6A). The labeling of KC2 in the liver of *Ms4a3*^{cre} x *Rosa*^{Tomato} mice under HFD increased after 18 weeks, suggesting that the growth of the KC2 population was partially dependent on monocyte recruitment only at late time points of HFD (Figures S6A and S6B). We then compared the transcriptomic profiles of the two populations of KCs sorted from mice fed a HFD for 2 months. The dichotomy between the two KC subpopulations was conserved (Figure S6C), even if we noticed that both acquired a more pronounced metabolic-oriented signature upon HFD (Figures 6C–6E and S6D). Notably, genes involved in fatty acid processing were upregulated, and the ones related to amino acid catabolism were downregulated, in KC2. We found *Cd36* among the genes upregulated upon HFD, a gene extensively described in the literature for its role in lipid uptake and oxidative stress modulation in macrophages (Kunjathoor et al., 2002; Silverstein and Febbraio, 2009).

Accordingly, we checked the expression of *Cd36* by KC2 in a recently and independently published murine liver single-cell RNA-seq dataset (Kolodziejczyk et al., 2020). By focusing on the *Clec4f*$^{+}$ KC population, we observed that *Cd36* was more expressed in *Mrc1*$^{+}$ KCs (Figure 6F). We then used conventional flow cytometry to validate these transcriptomic results and observed that the CD36 marker signal was indeed strongly elevated in KC2 compared to KC1 at steady state and was upregulated upon HFD (Figure 6G). These data highlighted KC2 as a metabolically responsive macrophage population with lipid handling being modulated during diet-induced obesity.

CD36-specific targeting in KCs modulates liver metabolism

To further study the role of KC2 in liver metabolism, we finally adopted an interventional approach by targeting KC2 in the context of metabolic challenges induced by HFD. As all macrophage-oriented fate-mapping models failed to discriminate KC1 and KC2, we were unable to specifically target KC2 with these tools. Therefore, we used our pan-omics signatures (Figure 5) to identify KC2-specific markers that could be used to target them and to investigate their functional significance in HFD-fed mice. *Cdh5* is considered as a core KC gene (Scott et al., 2018), but in parallel, the *Cdh5*^{creERT2} x *Rosa*^{Tomato} model has been successfully used to label endothelial cells (Gentek et al., 2018). *Cdh5* was more expressed in KC2 both at RNA and protein levels, and KC2, but not KC1, were specifically tagged in *Cdh5*^{creERT2} x *Rosa*^{Tomato} mice fed with tamoxifen for 7 days (Figure S7A). Of note, the labeling of the two subsets was very stable across time, with no observed changes for 13 weeks post-tamoxifen treatment, excluding a conversion from one subset to another one at steady state. Therefore, we made *Cdh5*^{creERT2} *x Rosa*^{DTR} mice and generated chimeras (*Cdh5*^{creERT2} *x Rosa*^{DTR} bone marrow engrafted into WT recipients to avoid targeting of radioresistant LSECs that also express *Cdh5*) to establish a system allowing inducible and specific depletion of KC2 (Figure S7B). After tamoxifen induction, we validated this system by injecting *Diphteria* toxin (DT) into tamoxifen-treated chimeric *Cdh5*^{creERT2} *x Rosa*^{DTR} mice and followed the kinetics of KC2 depletion. Tim4^{+} CD206^{hi} ESAM^{+} KC2, but not Tim4^{+} CD206^{lo} ESAM^{-} KC1, were efficiently depleted after a single injection of DT (Figure S7C), while adipose tissue macrophages were not impacted (Figure S7D), supporting the specificity of such a strategy to target KC2.

We then fed tamoxifen- and DT- treated *Cdh5*^{creERT2} *x Rosa*^{DTR} chimeras (KC2-deficient group) with HFD for weeks to assess the role of KC2 in the HFD-driven metabolic changes. HFD did not induce any weight gain in KC2-deficient animals, while KC2-sufficient animals gained weight over the period of HFD (Figures 7A and S7E). Considering the noticeable regulation of genes involved in lipid metabolism and oxidative stress in KC2 upon HFD feeding, we monitored the amounts of both reactive oxygen species (ROS) H_2O_2, which is a well-known marker of oxidative stress, and the lipid peroxidation by-product malondialdehyde (MDA) following KC2 depletion. As expected, HFD induced an increase of ROS and MDA (Figure 7B) (Azzimato et al., 2020). However, KC2 depletion resulted in a decrease of both ROS and MDA, suggesting that KC2 could contribute to hepatic lipid peroxidation and oxidative stress associated with obesity. This was accompanied by improved glucose tolerance and a less-pronounced steatosis in KC2-depleted animals (Figures 7C, 7D, S7F, and S7G). However, even if metabolic impairments including obesity, oxidative stress, steatosis, and glucose intolerance were reduced, serum concentration of triglycerides (TGs) was increased (Figure 7E). In line with these results, indirect calorimetric measurements revealed that KC2-depleted animals had lower food intake, higher energy expenditure related to respiratory exchange ratio of VO_2 and VCO_2, and increased locomotor activity compared to KC2-sufficient animals during the early phase of HFD (Figures 7F, 7G, and S7H). Considering the entanglement of metabolic functions between different organs including the liver, pancreas, adipose tissue, and brain, these observations could reflect a profound metabolic rewiring consecutive to KC2 depletion and would deserve future detailed investigations.

But to circumvent such possible systemic effects, we finally used a more targeted strategy based on glucan-encapsulated small interfering RNA (siRNA) particles (GeRPs) for specific silencing of *Cd36* in KCs (Aouadi et al., 2009; Barreby et al., 2019). While we had previously shown that GeRPs are specifically delivered to macrophages in the liver, but not to macrophages or other cells in other organs (Azzimato et al., 2020; Jourdan et al., 2017; Morgantini et al., 2019; Tencerova et al., 2015),

(C) Heatmap of the DEGs between the two populations.
(D–F) Same analysis as in (A)–(C), but with the translatomes obtained from *Lyz2*^{cre} x *Rpl22*^{HA} mice (RiboTag approach).
(G–I) Same analysis as in (A)–(C), but with proteomes.
(J) Principal-component analysis of the integrated transcriptome, translatome, and proteome datasets.
(K) Heatmap of the top 10 metabolism-related DEGs between KC1 and KC2.
See also Figure S5.

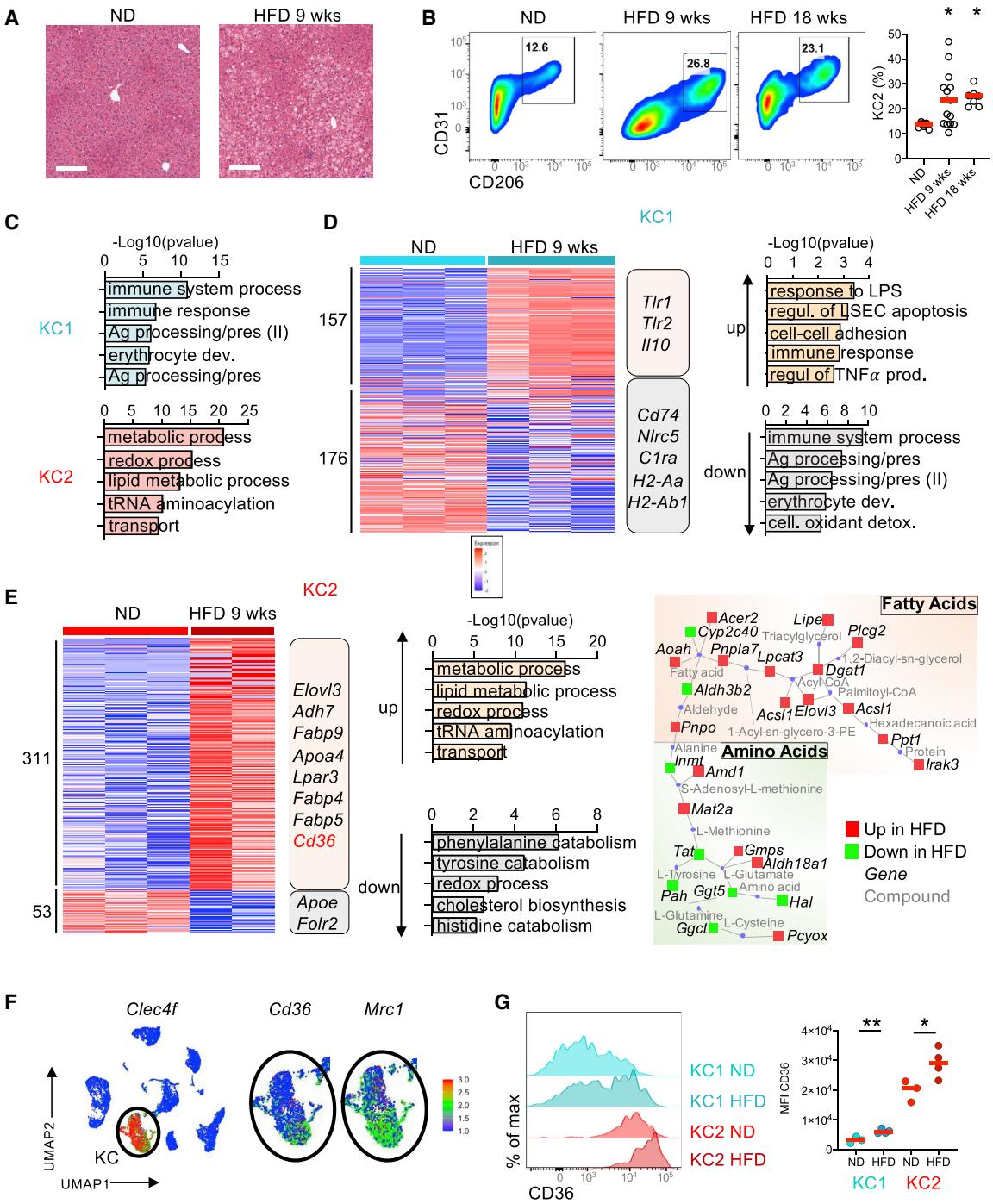

Figure 6. KC2 exhibit metabolic functions

(A) Images of H&E staining of normal diet (ND)- or high-fat diet (HFD)-fed mouse livers after 9 weeks of diet.

(B) Flow cytometry plots showing the frequency of KC1 and KC2 among KCs in mice fed with HFD for the indicated time. Each dot represents an individual, and the median is indicated by a red line.

(C) Pathway analysis using total DEGs between KC1 and KC2 sorted from ND- and HFD-fed mice.

(D) Heatmap and pathway analysis of the DEGs between KC1 sorted from ND and HFD mice. Canonical DEGs are displayed in the boxes.

(E) Heatmap and pathway analysis of the DEGs between KC2 sorted from ND and HFD mice. Canonical DEGs are displayed in the boxes, and integrated network analysis of DEGs between ND and HFD is provided.

(F) Single-cell RNA-seq data (55, 118 cells) were extracted from Kolodziejczyk et al. (2020). KCs were identified according to their high expression of *Clec4f*. *Cd36* and *Mrc1* expressions are overlaid on the KC population.

(G) Flow cytometry profiles of the intensity of expression of CD36 on the indicated populations and quantification of the mean fluorescence intensity (MFI). See also Figure S6.

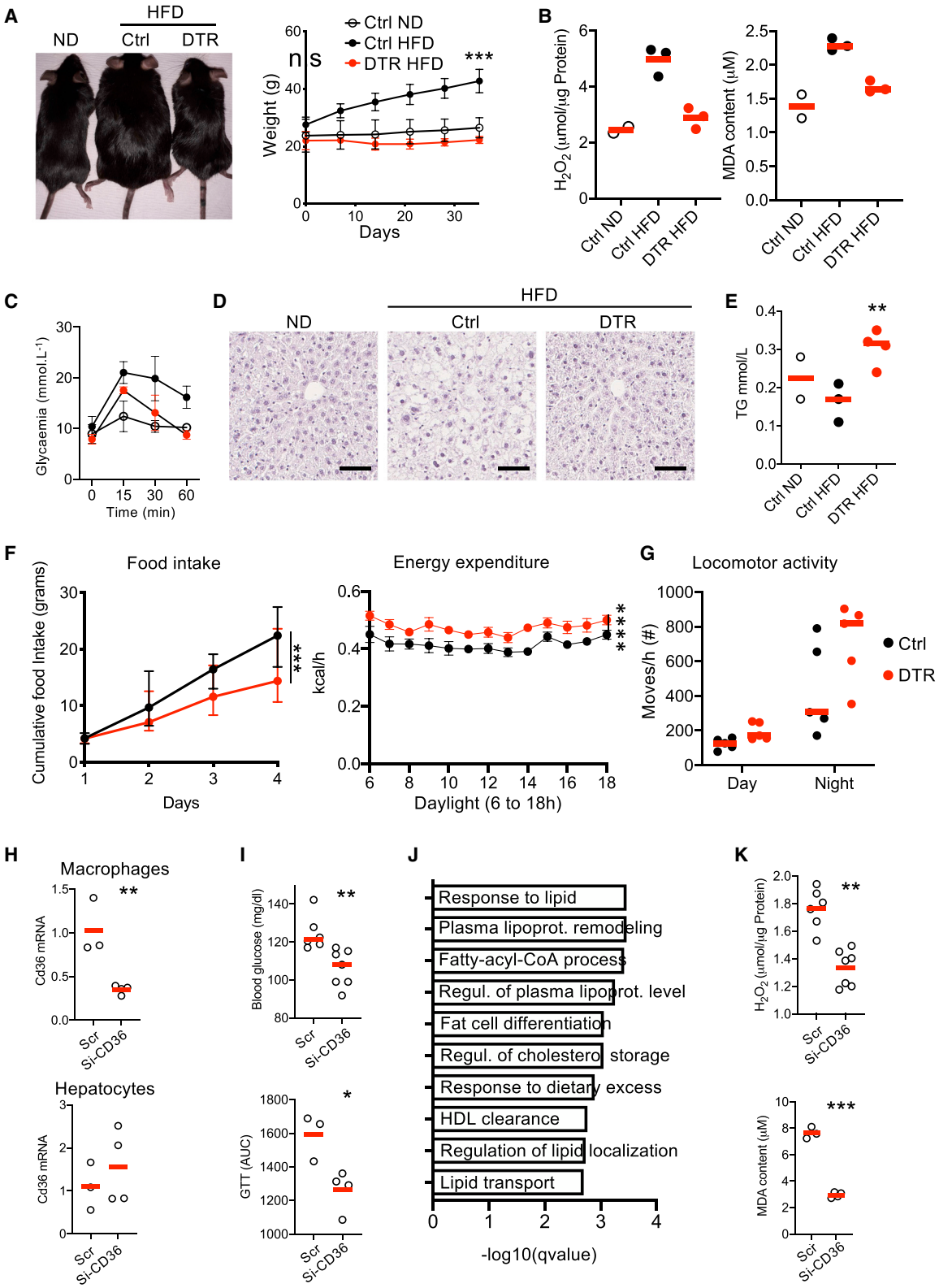

Figure 7. CD36 is involved in KC2 modulation of liver metabolism

(A) Absolute weight in control and KC2-depleted mice during the 6 first weeks of HFD.

(B) Hydrogen peroxide and malondialdehyde assays in the liver of the indicated mice.

(C) Glucose tolerance test was performed on overnight fasted mice during week 6 of HFD.

(legend continued on next page)

we first used FITC-GeRPs to verify the specificity of the targeting within the hepatic cell populations. When intravenously injected, FITC-GeRPs were retrieved only in KC1 and KC2 and not in other liver cells such as LSECs and monocytes, confirming the equal phagocytic abilities of both KC subpopulations (Figure S7I). Then, mice were fed a HFD for 7 weeks and treated with GeRPs loaded with either a control scrambled siRNA or a *Cd36* targeting siRNA for 2 weeks. This treatment allowed for the short-term specific silencing of *Cd36* in KCs (Figure 7H). *Cd36* expression remained unchanged in monocytes and adipose tissue macrophages, confirming the specific delivery of GeRPs to KCs (Figure S7J). Even if we did not observe any significant effect on weight gain during the 2-week treatment period (Figure S7K), both glycaemia and glucose tolerance were improved in *Cd36* siRNA-treated animals (Figure 7I). To further investigate the effect of *Cd36* on KC phenotype, we then analyzed their transcriptomic profile following *Cd36* silencing and observed a modulation of genes involved in lipid metabolism (Figure 7J).

Finally, we tested the effect of *Cd36* silencing on hepatic ROS and MDA concentrations. Consistent with our hypothesis, *Cd36* silencing decreased accumulation of both MDA and ROS (Figures 7K and S7L). This occurred independently of liver TG content (Figure S7M). Taken together, these data highlight a pivotal role of CD36 specifically expressed by KC2 in obese mice for liver metabolic homeostasis regulation.

DISCUSSION

Herein, we report the presence of two phenotypically and functionally distinct subsets of KCs in the healthy murine liver. The liver is now recognized as a common niche for several macrophage populations, but these two populations of KCs share a common embryonic origin, clearly differentiating them from the other monocyte-derived liver macrophages (Blériot and Ginhoux, 2019). KC1 and KC2 are present at steady state and are not the result of the recruitment of monocytes, which occurs neonatally or in inflammatory conditions (Blériot et al., 2015; Scott et al., 2016). These two populations share the common core macrophage signature with a high expression of well-known KC-core markers including *Clec4f*, *Lyz2*, or *Csf1r*, while KC2 additionally express a set of genes previously thought to be restricted to LSECs.

These results are in line with a previous study showing that cultured primary KCs share several functional antigens with LSECs (Okada et al., 2016); however, the global approach used in the mentioned study did not allow the detection of a specific subpopulation of KCs. Although recent work has detected potential contamination of KC populations by LSECs using conventional flow cytometry (Lynch et al., 2018), we were able to identify and exclude this minor contamination in our single-cell RNA-seq dataset. Thus, the KC2 population that we identified is composed of bona fide KCs, evidenced by fate-mapping models and the high expression of macrophage-core genes. In line with our study, the existence of a CD206$^+$ population of KCs has been already reported (David et al., 2016; Han et al., 2017; Wan et al., 2014) and even suggested in humans in a recently published study (Wu et al., 2020). Furthermore, a Lyve1$^+$CD206$^+$ population of macrophages harboring similarities with KC2 is also present in atherosclerotic plaques, suggesting that such "metabolic" macrophages could actually be present in other niches than the liver (Kim et al., 2018). Of note, a role in active phagocytosis of blood-borne cellular material has been proposed for the CD206$^+$ macrophages (A-Gonzalez et al., 2017). Together, these data argue for a central role of this receptor in macrophage biology, and CD206 should be systematically included in future analyses of these cells. This also parallels our recent findings of two populations of lung interstitial macrophages and across tissues discriminated by differential Lyve1 and CD206 expression (Chakarov et al., 2019). The other important biomarker that we have identified is ESAM. This molecule, whose expression was thought to be restricted to LSECs, is also expressed by a subset of splenic DCs (Lewis et al., 2011), but until now was not thought to be expressed by macrophages. Although *Lyve1*, *Cd206*, and *Esam* have been long considered as endothelial-restricted genes, our results in the liver and previous ones in other organs are revisiting this concept and clearly show that these genes can also be expressed by RTMs, even if the complete functional roles of these markers in RTMs need to be further investigated.

The dichotomy between CD206$^-$ and CD206$^+$ populations is completely independent of the origin of the macrophages (i.e., monocyte- or embryonically derived) and should be dictated only by the niche of residence, reinforcing the concept of the niche being one dominant factor driving macrophage identity (Blériot et al., 2020a; Guilliams and Scott, 2017). However, here, we have failed to identify a distinct sub-liver niche for each subset. Metabolic zonation in the liver is important and shapes the transcriptomic pattern of hepatocytes (Halpern et al., 2017) and LSECs (Halpern et al., 2018), but KC1 and KC2 seem to be randomly distributed within the acini. Thus, their polarization is likely linked to unknown factors other than oxygen or nutrient availability. Identification of these determinants is a considerable challenge and should extend our comprehension of what we can call the distinct "niches" present within the liver. This also stresses the need to investigate the heterogeneity of the other different cell types of the liver, including stellate cells and LSECs, that could contribute to KC1 versus KC2 identity.

(D) H&E staining of liver slices from indicated mice.
(E) Measurement of circulating TGs in indicated mice.
(F and G) Mice were placed individually in metabolic cages during the first week of the HFD, and energy intake and expenditures were measured.
(H) Mice were injected with GeRPs containing scrambled RNA (Scr) or siRNA directed against *Cd36* (si-CD36) three times a week for 2 weeks, and *Cd36* expression was assessed by qPCR at the end of the treatment on indicated sorted cells.
(I) Glycemia and glucose tolerance test (GTT) were measured at the end of the treatment.
(J) Bulk RNA-seq was performed on total liver macrophages. Data from CD36 KD and Scr-treated mice were compared, and pathways modulated are displayed.
(K) Measurement of oxidative stress markers MDA and H_2O_2 in the liver of the same mice. Each dot represents an individual, and the median is indicated by a red line.
For (A)–(G), two independent experiments were conducted. Groups were composed of 3–4 mice. See also Figure S7.

Indeed, recent studies in a mouse model of depletion of embryonic KCs have shown that liver-entering monocytes were reprogrammed into KC-like cells via crosstalk with hepatic stellate and LSECs (Bonnardel et al., 2019; Sakai et al., 2019). These two studies have identified a key liver triptych composed of hepatic stellate cells, LSECs, and macrophages. Therefore, deciphering the crosstalk among these three different cell types and their potential subpopulations and, notably, its modulation in the context of different liver pathologies will be a challenge for further studies.

In the context of the KC subsets identified here, we want to emphasize that KC2 are already present in the steady state and are poised to respond to metabolic challenges. Therefore, determining how this cell identity is generated will be useful for understanding liver pathologies, considering that almost a quarter of the human population is affected by NAFLDs (Lonardo et al., 2016; Younossi et al., 2016). In line with this, the cellular liver triptych also seems to be present in humans, as evidenced by the identification of key ''stellakines,'' which are secreted by hepatic stellate cells during NASH (Xiong et al., 2019) and cirrhosis (Ramachandran et al., 2019) and impact macrophage biology. As exemplified in these two elegant studies, the recent progress of single-cell transcriptomics and the subsequent release of several atlases in both mouse (Han et al., 2018; Tabula Muris Consortium, 2018) and human (Aizarani et al., 2019; MacParland et al., 2018; Mulder et al., 2021; Ramachandran et al., 2019; Sharma et al., 2020) will improve our knowledge of hepatology and liver diseases, even if the existence of corresponding functionally distinct KC1 and KC2 populations in humans remains to be formally established.

Functionally, we identified a specific metabolic role for KC2. However, it would be misleading to claim that only KC2 are involved in liver metabolism regulation. Our data, rather, highlight that both KC subpopulations participate to this function, even if KC2 population seems to be more wired to do so. Furthermore, it is noticeable that KC2 are present in steady state and do not depend on the monocyte recruitment that occurs in the late stages of obesity. In line with this, a previous study indicated a central role of liver macrophages in metabolism considering KCs as a homogeneous population (Morgantini et al., 2019). The authors showed that the non-inflammatory factor insulin-like growth factor-binding protein 7 (IGFBP7) was important in metabolic regulation by KCs. Importantly, in addition to *Cd36*, we observed that *Igfbp7* was among the top DEGs between KC1 and KC2, being highly overexpressed in KC2. Hence, it is tempting to hypothesize that the effect reported in the aforementioned study could be mostly driven by the KC2 population. In addition, we provide direct evidence for a role of the KC2-expressed receptor CD36 in liver metabolism regulation. These results are perfectly in line with the emerging central role of CD36 in NASH development and obesity-related disorders (Rada et al., 2020). While further investigations are needed to better understand the systemic effect of KC2 depletion, our targeted approach to silence the lipid transporter CD36 revealed an important role of these cells in the regulation of glucose homeostasis and oxidative stress. It has been previously reported that decreasing oxidative stress in KCs in obesity can improve liver metabolism and decrease ROS concentrations (Azzimato et al., 2020). Here, we refine this observation by showing that KC2 play a major role in this process by processing lipids via CD36.

However, we should recognize that a precise understanding of NASH etiology is not yet achieved and that humans probably develop a spectrum of convergent diseases. So, we cannot exclude that KCs could be differentially involved in other experimental models of NASH. For example, it has been shown that inflammatory monocytes enter the liver and induce transient changes in liver macrophage homeostasis in a NASH model induced by a methionine-choline-deficient (MCD) diet (Devisscher et al., 2017). Furthermore, very recent studies using different diets report that embryonically derived KCs disappeared after several weeks and were replaced by a population of monocyte-derived lipid-associated macrophages (LAMs) linked with the development of pathologies (Remmerie et al., 2020; Seidman et al., 2020; Tran et al., 2020) and comparable to those already reported in adipose tissue from obese individuals (Jaitin et al., 2019). However, these studies used essentially rodent-based models, which, by definition, can be limited in their abilities to mimic human diseases. As an example, MCD-induced NASH is associated with a severe and quick loss of weight, liver inflammation, and subsequent fibrosis. Even if the latter could be close to the human situation, the first is not observed clinically and might be responsible for model-specific side effects. On the contrary, HFD-induced NASH could reflect more human-obesity-induced disorders but is less efficient to induce liver fibrosis. So, it appears fundamental to remind that there is not yet a model universally recognized to fully recapitulate human NAFLD/NASH (Hebbard and George, 2011). This being said, the model of HFD that we used herein does not induce a significant recruitment of monocytes in the liver at early stages. So, while most of the studies were focused on monocyte-derived LAMs recruited in the metabolically challenged liver, our study indicates that a fraction of embryonic KCs is already fated to assume metabolic functions. Further studies should refine their precise roles in this context or even in other ones, allowing for the design of innovative therapies targeting metabolic function of KC2 for the modulation of liver metabolic diseases.

Finally, in parallel to the current study in which we described the two distinct KC1 and KC2 populations and KC2 metabolic functions, we have investigated their capacities to present antigens in a mouse model of hepatitis B virus pathogenesis. This has revealed key differences between the two populations, with KC2 being notably responsive to interleukin (IL)-2 signaling and involved in mounting efficient T-cell-mediated responses to hepatocellular antigens (De Simone et al., 2021). This study reports a specific effect of the KC2 subpopulation in mounting immune responses and validates our approach of investigating heterogeneity of tissue-resident macrophage populations. Indeed, even if the literature often assumes that macrophages from one common tissue compose a uniform population, our data reported here and previously (Chakarov et al., 2019) have shown that sub-tissular niches exist, inhabited by different macrophage populations. Thus, development of macrophage-based therapeutic strategies will have to take this heterogeneity into account to improve the specificity and efficiency of innovative treatments.

Limitations of study

While we extensively describe here a discrete metabolic subset of KCs, our data have been generated by using rodent models. Future investigations would, therefore, have to validate these findings in human subjects. Indeed, even if the first reports have already confirmed human KC heterogeneity (MacParland et al., 2018; Ramachandran et al., 2019; Wu et al., 2020; Xiong et al., 2019), analysis of this KC heterogeneity with a metabolism focus remains to be performed. In addition, the description of KC2 metabolic functions can appear limited here, and more in-depth approaches should be applied to dissect how KC2 and related cells in other tissues (e.g., adipose tissue, brain) are integrated in a global metabolic regulation of the organism.

STAR★METHODS

Detailed methods are provided in the online version of this paper and include the following:

- KEY RESOURCES TABLE
- RESOURCE AVAILABILITY
  - Lead contact
  - Materials availability
  - Data and code availability
- METHOD DETAILS
  - Animal models
  - Cell preparation
  - Transcriptomics
  - Imaging
- QUANTIFICATION AND STATISTICAL ANALYSIS

SUPPLEMENTAL INFORMATION

Supplemental information can be found online at https://doi.org/10.1016/j.immuni.2021.08.006.

ACKNOWLEDGMENTS

We thank all the members of the Ginhoux laboratory for helpful discussions. Flow cytometry and cell sorting, CyTOF, microscopy, and RNA library preparation were carried out on SIgN platforms established by the Agency of Science, Technolog,y and Research (A*STAR) Singapore. We would like to acknowledge C. Phua and the staff from the Biological Resource Center for their invaluable help for the animal-based experiments and the Electron Microscopy Unit, National University of Singapore, particularly Professor Ong Wei Yi, Miss Tan Suat Hoon, and Mister Lu Thong Beng. We would like to thank L. Robinson of Insight Editing London for editing the manuscript. SIgN platforms are supported by a BMRC IAF311006 grant and BMRC transition funds #H16/99/b0/011. This project has received funding from the European Research Council (ERC) under the European Union's Horizon 2020 research and innovation programme (grant agreement no. 864788). This work was supported by EMBO YIP, Singapore Immunology Network core funding (A*STAR), and Singapore NRF Senior Investigatorship (NRFI2017-02) to F.G.; A*STAR core funding and Singapore NRF under its NRF-SIS "SingMass" scheme to R.M.S.; NUHS start-up funding (NUHSRO/ 2018/006/SU/01) to B.M.; and ARC and FRM programs to C.B. N.V. was supported by the European Union Horizon 20202 (H2020) framework (ERC-EpiFAT 725790).

AUTHOR CONTRIBUTIONS

Conception, C.B. and F.G.; research design and experimentation, C.B., E.B., G.D., R.B., S.C., X.F., G.D.S., F.A., V.F., W.G., G.W., G.G., A.K., X.M.Z., N.A., P.C., C.M., V.A., W.T.K., Z.L., R.P., J.L., F.S., I.L., C.X., B.M., M.F.M.K., A.B., O.C., W.W.P., R.M.S., L.Y.-C., N.V., M.I., M.A., and F.G.; data analysis, C.B., S.C., G.W., X.F., G.D.S., F.A., V.F., G.G., A.K., X.M.Z., W.T.K., W.G., Z.L., and F.G.; resource assistance, A.L., B.L., E.W.N., L.G.N., S.W.H., J.C., and M.B.; writing of draft and editing, C.B. and F.G.; project administration, F.G.

DECLARATION OF INTERESTS

C.B., M.A., and F.G. are inventors on a patent filed, owned, and managed by A*ccelerate technologies Pte Ltd, A-STAR, Singapore, on technology related to the work presented in this manuscript.

Received: December 4, 2020
Revised: April 27, 2021
Accepted: August 9, 2021
Published: August 31, 2021

REFERENCES

A-Gonzalez, N., Quintana, J.A., García-Silva, S., Mazariegos, M., González de la Aleja, A., Nicolás-Ávila, J.A., Walter, W., Adrover, J.M., Crainiciuc, G., Kuchroo, V.K., et al. (2017). Phagocytosis imprints heterogeneity in tissue-resident macrophages. J. Exp. Med. *214*, 1281–1296.

Aibar, S., González-Blas, C.B., Moerman, T., Huynh-Thu, V.A., Imrichova, H., Hulselmans, G., Rambow, F., Marine, J.C., Geurts, P., Aerts, J., et al. (2017). SCENIC: single-cell regulatory network inference and clustering. Nat. Methods *14*, 1083–1086.

Aizarani, N., Saviano, A., Sagar, Mailly, L., Durand, S., Herman, J.S., Pessaux, P., Baumert, T.F., and Grün, D. (2019). A human liver cell atlas reveals heterogeneity and epithelial progenitors. Nature *572*, 199–204.

Andrikopoulos, S., Blair, A.R., Deluca, N., Fam, B.C., and Proietto, J. (2008). Evaluating the glucose tolerance test in mice. Am. J. Physiol. Endocrinol. Metab. *295*, E1323–E1332.

Aouadi, M., Tesz, G.J., Nicoloro, S.M., Wang, M., Chouinard, M., Soto, E., Ostroff, G.R., and Czech, M.P. (2009). Orally delivered siRNA targeting macrophage Map4k4 suppresses systemic inflammation. Nature *458*, 1180–1184.

Aparicio-Vergara, M., Tencerova, M., Morgantini, C., Barreby, E., and Aouadi, M. (2017). Isolation of Kupffer Cells and Hepatocytes from a Single Mouse Liver. Methods Mol. Biol. *1639*, 161–171.

Azzimato, V., Jager, J., Chen, P., Morgantini, C., Levi, L., Barreby, E., Sulen, A., Oses, C., Willerbrords, J., Xu, C., et al. (2020). Liver macrophages inhibit the endogenous antioxidant response in obesity-associated insulin resistance. Sci. Transl. Med. *12*, eaaw9709.

Barreby, E., Sulen, A., and Aouadi, M. (2019). Glucan-Encapsulated siRNA Particles (GeRPs) for Specific Gene Silencing in Adipose Tissue Macrophages. Methods Mol. Biol. *1951*, 49–57.

Beattie, L., Sawtell, A., Mann, J., Frame, T.C.M., Teal, B., de Labastida Rivera, F., Brown, N., Walwyn-Brown, K., Moore, J.W.J., MacDonald, S., et al. (2016). Bone marrow-derived and resident liver macrophages display unique transcriptomic signatures but similar biological functions. J. Hepatol. *65*, 758–768.

Becht, E., McInnes, L., Healy, J., Dutertre, C.A., Kwok, I.W.H., Ng, L.G., Ginhoux, F., and Newell, E.W. (2018). Dimensionality reduction for visualizing single-cell data using UMAP. Nat Biotechnol. https://doi.org/10.1038/nbt.4314.

Blériot, C., Chakarov, S., and Ginhoux, F. (2020a). Determinants of Resident Tissue Macrophage Identity and Function. Immunity *52*, 957–970.

Blériot, C., Dupuis, T., Jouvion, G., Eberl, G., Disson, O., and Lecuit, M. (2015). Liver-resident macrophage necroptosis orchestrates type 1 microbicidal inflammation and type-2-mediated tissue repair during bacterial infection. Immunity *42*, 145–158.

Blériot, C., and Ginhoux, F. (2019). Understanding the Heterogeneity of Resident Liver Macrophages. Front. Immunol. *10*, 2694.

Blériot, C., Li, S., Kairi, M.F.B.M., Newell, E., and Ginhoux, F. (2020b). Kupffer Cell Characterization by Mass Cytometry. Methods Mol. Biol. *2164*, 87–99.

Bonnardel, J., T'Jonck, W., Gaublomme, D., Browaeys, R., Scott, C.L., Martens, L., Vanneste, B., De Prijck, S., Nedospasov, S.A., Kremer, A., et al. (2019). Stellate Cells, Hepatocytes, and Endothelial Cells Imprint the Kupffer

Cell Identity on Monocytes Colonizing the Liver Macrophage Niche. Immunity *51*, 638–654.e9.

Butler, A., Hoffman, P., Smibert, P., Papalexi, E., and Satija, R. (2018). Integrating single-cell transcriptomic data across different conditions, technologies, and species. Nat. Biotechnol. *36*, 411–420.

Chakarov, S., Lim, H.Y., Tan, L., Lim, S.Y., See, P., Lum, J., Zhang, X.M., Foo, S., Nakamizo, S., Duan, K., et al. (2019). Two distinct interstitial macrophage populations coexist across tissues in specific subtissular niches. Science *363*, eaau0964.

Chen, H., Lau, M.C., Wong, M.T., Newell, E.W., Poidinger, M., and Chen, J. (2016). Cytofkit: A Bioconductor Package for an Integrated Mass Cytometry Data Analysis Pipeline. PLoS Comput. Biol. *12*, e1005112.

Cheng, Y., Wong, M.T., van der Maaten, L., and Newell, E.W. (2016). Categorical Analysis of Human T Cell Heterogeneity with One-Dimensional Soli-Expression by Nonlinear Stochastic Embedding. J. Immunol. *196*, 924–932.

David, B.A., Rezende, R.M., Antunes, M.M., Santos, M.M., Freitas Lopes, M.A., Diniz, A.B., Sousa Pereira, R.V., Marchesi, S.C., Alvarenga, D.M., Nakagaki, B.N., et al. (2016). Combination of Mass Cytometry and Imaging Analysis Reveals Origin, Location, and Functional Repopulation of Liver Myeloid Cells in Mice. Gastroenterology *151*, 1176–1191.

De Simone, G., Andreata, F., Bleriot, C., Fumagalli, V., Laura, C., Garcia-Manteiga, J.M., Di Luca, P., Gilotto, S., Ficht, X., De Ponti, F.F., et al. (2021). Identification of a Kupffer cell subset capable of reverting the T cell dysfunction induced by hepatocellular priming. Immunity *54*. Published online August 31, 2021. https://doi.org/10.1016/j.immuni.2021.05.005.

Devisscher, L., Scott, C.L., Lefere, S., Raevens, S., Bogaerts, E., Paridaens, A., Verhelst, X., Geerts, A., Guilliams, M., and Van Vlierberghe, H. (2017). Non-alcoholic steatohepatitis induces transient changes within the liver macrophage pool. Cell. Immunol. *322*, 74–83.

Dobin, A., Davis, C.A., Schlesinger, F., Drenkow, J., Zaleski, C., Jha, S., Batut, P., Chaisson, M., and Gingeras, T.R. (2013). STAR: ultrafast universal RNA-seq aligner. Bioinformatics *29*, 15–21.

Gebhardt, R. (1992). Metabolic zonation of the liver: regulation and implications for liver function. Pharmacol. Ther. *53*, 275–354.

Gentek, R., Ghigo, C., Hoeffel, G., Bulle, M.J., Msallam, R., Gautier, G., Launay, P., Chen, J., Ginhoux, F., and Bajénoff, M. (2018). Hemogenic Endothelial Fate Mapping Reveals Dual Developmental Origin of Mast Cells. Immunity *48*, 1160–1171.e5.

Guilliams, M., and Scott, C.L. (2017). Does niche competition determine the origin of tissue-resident macrophages? Nat. Rev. Immunol. *17*, 451–460.

Haimon, Z., Volaski, A., Orthgiess, J., Boura-Halfon, S., Varol, D., Shemer, A., Yona, S., Zuckerman, B., David, E., Chappell-Maor, L., et al. (2018). Re-evaluating microglia expression profiles using RiboTag and cell isolation strategies. Nat. Immunol. *19*, 636–644.

Halpern, K.B., Shenhav, R., Massalha, H., Toth, B., Egozi, A., Massasa, E.E., Medgalia, C., David, E., Giladi, A., Moor, A.E., et al. (2018). Paired-cell sequencing enables spatial gene expression mapping of liver endothelial cells. Nat. Biotechnol. *36*, 962–970.

Halpern, K.B., Shenhav, R., Matcovitch-Natan, O., Toth, B., Lemze, D., Golan, M., Massasa, E.E., Baydatch, S., Landen, S., Moor, A.E., et al. (2017). Single-cell spatial reconstruction reveals global division of labour in the mammalian liver. Nature *542*, 352–356.

Han, X., Wang, R., Zhou, Y., Fei, L., Sun, H., Lai, S., Saadatpour, A., Zhou, Z., Chen, H., Ye, F., et al. (2018). Mapping the Mouse Cell Atlas by Microwell-Seq. Cell *172*, 1091–1107.e17.

Han, Y.H., Kim, H.J., Na, H., Nam, M.W., Kim, J.Y., Kim, J.S., Koo, S.H., and Lee, M.O. (2017). RORα Induces KLF4-Mediated M2 Polarization in the Liver Macrophages that Protect against Nonalcoholic Steatohepatitis. Cell Rep. *20*, 124–135.

Hashimoto, D., Chow, A., Noizat, C., Teo, P., Beasley, M.B., Leboeuf, M., Becker, C.D., See, P., Price, J., Lucas, D., et al. (2013). Tissue-resident macrophages self-maintain locally throughout adult life with minimal contribution from circulating monocytes. Immunity *38*, 792–804.

Hebbard, L., and George, J. (2011). Animal models of nonalcoholic fatty liver disease. Nat. Rev. Gastroenterol. Hepatol. *8*, 35–44.

Hoeffel, G., Chen, J., Lavin, Y., Low, D., Almeida, F.F., See, P., Beaudin, A.E., Lum, J., Low, I., Forsberg, E.C., et al. (2015). C-Myb(+) erythro-myeloid progenitor-derived fetal monocytes give rise to adult tissue-resident macrophages. Immunity *42*, 665–678.

Jaitin, D.A., Adlung, L., Thaiss, C.A., Weiner, A., Li, B., Descamps, H., Lundgren, P., Bleriot, C., Liu, Z., Deczkowska, A., et al. (2019). Lipid-Associated Macrophages Control Metabolic Homeostasis in a Trem2-Dependent Manner. Cell *178*, 686–698.e14.

Jourdan, T., Nicoloro, S.M., Zhou, Z., Shen, Y., Liu, J., Coffey, N.J., Cinar, R., Godlewski, G., Gao, B., Aouadi, M., et al. (2017). Decreasing CB_1 receptor signaling in Kupffer cells improves insulin sensitivity in obese mice. Mol. Metab. *6*, 1517–1528.

Jungermann, K., and Saase, D. (1978). Heterogeneity of liver parenchymal cells. Trends Biochem. Sci. *3*, 198–202.

Kim, K., Shim, D., Lee, J.S., Zaitsev, K., Williams, J.W., Kim, K.W., Jang, M.Y., Seok Jang, H., Yun, T.J., Lee, S.H., et al. (2018). Transcriptome Analysis Reveals Nonfoamy Rather Than Foamy Plaque Macrophages Are Proinflammatory in Atherosclerotic Murine Models. Circ. Res. *123*, 1127–1142.

Klein, I., Cornejo, J.C., Polakos, N.K., John, B., Wuensch, S.A., Topham, D.J., Pierce, R.H., and Crispe, I.N. (2007). Kupffer cell heterogeneity: functional properties of bone marrow derived and sessile hepatic macrophages. Blood *110*, 4077–4085.

Kolodziejczyk, A.A., Federici, S., Zmora, N., Mohapatra, G., Dori-Bachash, M., Hornstein, S., Leshem, A., Reuveni, D., Zigmond, E., Tobar, A., et al. (2020). Acute liver failure is regulated by MYC- and microbiome-dependent programs. Nat. Med. *26*, 1899–1911.

Krenkel, O., and Tacke, F. (2017). Liver macrophages in tissue homeostasis and disease. Nat. Rev. Immunol. *17*, 306–321.

Kunjathoor, V.V., Febbraio, M., Podrez, E.A., Moore, K.J., Andersson, L., Koehn, S., Rhee, J.S., Silverstein, R., Hoff, H.F., and Freeman, M.W. (2002). Scavenger receptors class A-I/II and CD36 are the principal receptors responsible for the uptake of modified low density lipoprotein leading to lipid loading in macrophages. J. Biol. Chem. *277*, 49982–49988.

Lewis, K.L., Caton, M.L., Bogunovic, M., Greter, M., Grajkowska, L.T., Ng, D., Klinakis, A., Charo, I.F., Jung, S., Gommerman, J.L., et al. (2011). Notch2 receptor signaling controls functional differentiation of dendritic cells in the spleen and intestine. Immunity *35*, 780–791.

Li, B., and Dewey, C.N. (2011). RSEM: accurate transcript quantification from RNA-Seq data with or without a reference genome. BMC Bioinformatics *12*, 323.

Lim, H.Y., Lim, S.Y., Tan, C.K., Thiam, C.H., Goh, C.C., Carbajo, D., Chew, S.H.S., See, P., Chakarov, S., Wang, X.N., et al. (2018). Hyaluronan Receptor LYVE-1-Expressing Macrophages Maintain Arterial Tone through Hyaluronan-Mediated Regulation of Smooth Muscle Cell Collagen. Immunity *49*, 326–341.e7.

Liu, Z., Gu, Y., Chakarov, S., Bleriot, C., Kwok, I., Chen, X., Shin, A., Huang, W., Dress, R.J., Dutertre, C.A., et al. (2019). Fate Mapping via Ms4a3-Expression History Traces Monocyte-Derived Cells. Cell *178*, 1509–1525.e1519.

Lonardo, A., Byrne, C.D., Caldwell, S.H., Cortez-Pinto, H., and Targher, G. (2016). Global epidemiology of nonalcoholic fatty liver disease: Meta-analytic assessment of prevalence, incidence, and outcomes. Hepatology *64*, 1388–1389.

Lynch, R.W., Hawley, C.A., Pellicoro, A., Bain, C.C., Iredale, J.P., and Jenkins, S.J. (2018). An efficient method to isolate Kupffer cells eliminating endothelial cell contamination and selective bias. J. Leukoc. Biol. *104*, 579–586.

MacParland, S.A., Liu, J.C., Ma, X.Z., Innes, B.T., Bartczak, A.M., Gage, B.K., Manuel, J., Khuu, N., Echeverri, J., Linares, I., et al. (2018). Single cell RNA sequencing of human liver reveals distinct intrahepatic macrophage populations. Nat. Commun. *9*, 4383.

Mair, F., Erickson, J.R., Voillet, V., Simoni, Y., Bi, T., Tyznik, A.J., Martin, J., Gottardo, R., Newell, E.W., and Prlic, M. (2020). A Targeted Multi-omic

Analysis Approach Measures Protein Expression and Low-Abundance Transcripts on the Single-Cell Level. Cell Rep. *31*, 107499.

Mass, E., Ballesteros, I., Farlik, M., Halbritter, F., Günther, P., Crozet, L., Jacome-Galarza, C.E., Händler, K., Klughammer, J., Kobayashi, Y., et al. (2016). Specification of tissue-resident macrophages during organogenesis. Science *353*, aaf4238.

Morgantini, C., Jager, J., Li, X., Levi, L., Azzimato, V., Sulen, A., Barreby, E., Xu, C., Tencerova, M., Näslund, E., et al. (2019). Liver macrophages regulate systemic metabolism through non-inflammatory factors. Nat. Metab. *1*, 445–459.

Mulder, K., Patel, A.A., Kong, W.T., Piot, C., Halitzki, E., Dunsmore, G., Khalilnezhad, S., Irac, S.E., Dubuisson, A., Chevrier, M., et al. (2021). Cross-tissue single-cell landscape of human monocytes and macrophages in health and disease. Immunity *54*, 1883–1900.

Okada, T., Kimura, A., Kanki, K., Nakatani, S., Nagahara, Y., Hiraga, M., and Watanabe, Y. (2016). Liver Resident Macrophages (Kupffer Cells) Share Several Functional Antigens in Common with Endothelial Cells. Scand. J. Immunol. *83*, 139–150.

Picelli, S., Björklund, A.K., Faridani, O.R., Sagasser, S., Winberg, G., and Sandberg, R. (2013). Smart-seq2 for sensitive full-length transcriptome profiling in single cells. Nat. Methods *10*, 1096–1098.

Picelli, S., Faridani, O.R., Björklund, A.K., Winberg, G., Sagasser, S., and Sandberg, R. (2014). Full-length RNA-seq from single cells using Smart-seq2. Nat. Protoc. *9*, 171–181.

Rada, P., González-Rodríguez, Á., García-Monzón, C., and Valverde, A.M. (2020). Understanding lipotoxicity in NAFLD pathogenesis: is CD36 a key driver? Cell Death Dis. *11*, 802.

Ramachandran, P., Dobie, R., Wilson-Kanamori, J.R., Dora, E.F., Henderson, B.E.P., Luu, N.T., Portman, J.R., Matchett, K.P., Brice, M., Marwick, J.A., et al. (2019). Resolving the fibrotic niche of human liver cirrhosis at single-cell level. Nature *575*, 512–518.

Remmerie, A., Martens, L., Thoné, T., Castoldi, A., Seurinck, R., Pavie, B., Roels, J., Vanneste, B., De Prijck, S., Vanhockerhout, M., et al. (2020). Osteopontin Expression Identifies a Subset of Recruited Macrophages Distinct from Kupffer Cells in the Fatty Liver. Immunity *53*, 641–657.e14.

Ritchie, M.E., Phipson, B., Wu, D., Hu, Y., Law, C.W., Shi, W., and Smyth, G.K. (2015). limma powers differential expression analyses for RNA-sequencing and microarray studies. Nucleic Acids Res. *43*, e47.

Robinson, M.D., McCarthy, D.J., and Smyth, G.K. (2010). edgeR: a Bioconductor package for differential expression analysis of digital gene expression data. Bioinformatics. *26*, 139–140.

Sakai, M., Troutman, T.D., Seidman, J.S., Ouyang, Z., Spann, N.J., Abe, Y., Ego, K.M., Bruni, C.M., Deng, Z., Schlachetzki, J.C.M., et al. (2019). Liver-Derived Signals Sequentially Reprogram Myeloid Enhancers to Initiate and Maintain Kupffer Cell Identity. Immunity *51*, 655–670.e8.

Sanz, E., Yang, L., Su, T., Morris, D.R., McKnight, G.S., and Amieux, P.S. (2009). Cell-type-specific isolation of ribosome-associated mRNA from complex tissues. Proc. Natl. Acad. Sci. USA *106*, 13939–13944.

Schulz, C., Gomez Perdiguero, E., Chorro, L., Szabo-Rogers, H., Cagnard, N., Kierdorf, K., Prinz, M., Wu, B., Jacobsen, S.E., Pollard, J.W., et al. (2012). A lineage of myeloid cells independent of Myb and hematopoietic stem cells. Science *336*, 86–90.

Scott, C.L., T'Jonck, W., Martens, L., Todorov, H., Sichien, D., Soen, B., Bonnardel, J., De Prijck, S., Vandamme, N., Cannoodt, R., et al. (2018). The Transcription Factor ZEB2 Is Required to Maintain the Tissue-Specific Identities of Macrophages. Immunity *49*, 312–325.e5.

Scott, C.L., Zheng, F., De Baetselier, P., Martens, L., Saeys, Y., De Prijck, S., Lippens, S., Abels, C., Schoonooghe, S., Raes, G., et al. (2016). Bone marrow-derived monocytes give rise to self-renewing and fully differentiated Kupffer cells. Nat. Commun. *7*, 10321.

Seidman, J.S., Troutman, T.D., Sakai, M., Gola, A., Spann, N.J., Bennett, H., Bruni, C.M., Ouyang, Z., Li, R.Z., Sun, X., et al. (2020). Niche-Specific Reprogramming of Epigenetic Landscapes Drives Myeloid Cell Diversity in Nonalcoholic Steatohepatitis. Immunity *52*, 1057–1074.e7.

Sharma, A., Seow, J.J.W., Dutertre, C.A., Pai, R., Blériot, C., Mishra, A., Wong, R.M.M., Singh, G.S.N., Sudhagar, S., Khalilnezhad, S., et al. (2020). Onco-fetal Reprogramming of Endothelial Cells Drives Immunosuppressive Macrophages in Hepatocellular Carcinoma. Cell *183*, 377–394.e21.

Sierro, F., Evrard, M., Rizzetto, S., Melino, M., Mitchell, A.J., Florido, M., Beattie, L., Walters, S.B., Tay, S.S., Lu, B., et al. (2017). A Liver Capsular Network of Monocyte-Derived Macrophages Restricts Hepatic Dissemination of Intraperitoneal Bacteria by Neutrophil Recruitment. Immunity *47*, 374–388.e6.

Silverstein, R.L., and Febbraio, M. (2009). CD36, a scavenger receptor involved in immunity, metabolism, angiogenesis, and behavior. Sci. Signal. *2*, re3.

Stuart, T., Butler, A., Hoffman, P., Hafemeister, C., Papalexi, E., Mauck, W.M., 3rd, Hao, Y., Stoeckius, M., Smibert, P., and Satija, R. (2019). Comprehensive Integration of Single-Cell Data. Cell *177*, 1888–1902.e1821.

Tabula Muris Consortium (2018). Single-cell transcriptomics of 20 mouse organs creates a Tabula Muris. Nature *562*, 367–372.

Tencerova, M., Aouadi, M., Vangala, P., Nicoloro, S.M., Yawe, J.C., Cohen, J.L., Shen, Y., Garcia-Menendez, L., Pedersen, D.J., Gallagher-Dorval, K., et al. (2015). Activated Kupffer cells inhibit insulin sensitivity in obese mice. FASEB J. *29*, 2959–2969.

Tesz, G.J., Aouadi, M., Prot, M., Nicoloro, S.M., Boutet, E., Amano, S.U., Goller, A., Wang, M., Guo, C.A., Salomon, W.E., et al. (2011). Glucan particles for selective delivery of siRNA to phagocytic cells in mice. Biochem. J. *436*, 351–362.

Tran, S., Baba, I., Poupel, L., Dussaud, S., Moreau, M., Gélineau, A., Marcelin, G., Magréau-Davy, E., Ouhachi, M., Lesnik, P., et al. (2020). Impaired Kupffer Cell Self-Renewal Alters the Liver Response to Lipid Overload during Non-alcoholic Steatohepatitis. Immunity *53*, 627–640.e5.

van Rooijen, N., and Hendrikx, E. (2010). Liposomes for specific depletion of macrophages from organs and tissues. Methods Mol. Biol. *605*, 189–203.

Wan, J., Benkdane, M., Teixeira-Clerc, F., Bonnafous, S., Louvet, A., Lafdil, F., Pecker, F., Tran, A., Gual, P., Mallat, A., et al. (2014). M2 Kupffer cells promote M1 Kupffer cell apoptosis: a protective mechanism against alcoholic and nonalcoholic fatty liver disease. Hepatology *59*, 130–142.

Wang, C.Y., and Liao, J.K. (2012). A mouse model of diet-induced obesity and insulin resistance. Methods Mol. Biol. *821*, 421–433.

Wang, M., Huang, J., Liu, Y., Ma, L., Potash, J.B., and Han, S. (2017). COMBAT: A Combined Association Test for Genes Using Summary Statistics. Genetics. *207*, 883–891.

Wang, J., and Kubes, P. (2016). A Reservoir of Mature Cavity Macrophages that Can Rapidly Invade Visceral Organs to Affect Tissue Repair. Cell *165*, 668–678.

Wu, X., Hollingshead, N., Roberto, J., Knupp, A., Kenerson, H., Chen, A., Strickland, I., Horton, H., Yeung, R., Soysa, R., and Crispe, I.N. (2020). Human Liver Macrophage Subsets Defined by CD32. Front. Immunol. *11*, 2108.

Xiong, X., Kuang, H., Ansari, S., Liu, T., Gong, J., Wang, S., Zhao, X.Y., Ji, Y., Li, C., Guo, L., et al. (2019). Landscape of Intercellular Crosstalk in Healthy and NASH Liver Revealed by Single-Cell Secretome Gene Analysis. Mol. Cell *75*, 644–660.e5.

Yona, S., Kim, K.W., Wolf, Y., Mildner, A., Varol, D., Breker, M., Strauss-Ayali, D., Viukov, S., Guilliams, M., Misharin, A., et al. (2013). Fate mapping reveals origins and dynamics of monocytes and tissue macrophages under homeostasis. Immunity *38*, 79–91.

Younossi, Z.M., Koenig, A.B., Abdelatif, D., Fazel, Y., Henry, L., and Wymer, M. (2016). Global epidemiology of nonalcoholic fatty liver disease-Meta-analytic assessment of prevalence, incidence, and outcomes. Hepatology *64*, 73–84.

STAR★METHODS

KEY RESOURCES TABLE

REAGENT or RESOURCE	SOURCE	IDENTIFIER
Antibodies		
BUV395 Rat Anti-Mouse CD45	BD Biosciences	BD Biosciences Cat# 564279; RRID: AB_2651134
BV650 anti-mouse/human CD11b Antibody	BioLegend	BioLegend Cat# 101239; RRID: AB_11125575
PE-CF594 Hamster Anti-Mouse CD3e	BD Biosciences	BD Biosciences Cat# 562286; RRID: AB_11153307
PE-CF594 Rat Anti-Mouse CD19	BD Biosciences	BD Biosciences Cat# 562291; RRID: AB_11154223
PE-CF594 Rat Anti-Mouse Ly-6G	BD Biosciences	BD Biosciences Cat# 562700; RRID: AB_2737730
PE-CF594 Rat Anti-Mouse CD49b	BD Biosciences	BD Biosciences Cat# 562453; RRID: AB_11153857
APC/Cyanine7 anti-mouse F4/80 Antibody	BioLegend	BioLegend Cat# 123117; RRID: AB_893489
BV711 anti-mouse CD64 (FcγRI) Antibody	BioLegend	BioLegend Cat# 139311; RRID: AB_2563846
PE/Cyanine7 anti-mouse Tim-4 Antibody	BioLegend	BioLegend Cat# 130009; RRID: AB_2565718
AF700 anti-mouse I-A/I-E Antibody	BioLegend	BioLegend Cat# 107622; RRID: AB_493727
BV605 anti-mouse CD31 Antibody	BioLegend	BioLegend Cat# 102427; RRID: AB_2563982
PerCP/Cyanine5.5 anti-mouse Ly-6C Antibody	BioLegend	BioLegend Cat# 128012; RRID: AB_1659241
PE ESAM Monoclonal Antibody	Thermo Fisher Scientific	Thermo Fisher Scientific Cat# 12-5852-82; RRID: AB_891537
AF647 anti-mouse CD206 (MMR) Antibody	BioLegend	BioLegend Cat# 141712; RRID: AB_10900420
AF488 LYVE1 Monoclonal Antibody	Thermo Fisher Scientific	Thermo Fisher Scientific Cat# 53-0443-82; RRID: AB_1633415
PE/Cyanine7 anti-mouse CD36 Antibody	BioLegend	BioLegend Cat# 102615; RRID: AB_2566121
Anti-Mouse CD45 (30-F11)-89Y	Fluidigm	Fluidigm Cat# 3089005B; RRID: AB_2651152
CD19 Monoclonal Antibody (6D5)	Thermo Fisher Scientific	Thermo Fisher Scientific Cat# Q10379; RRID: AB_10563403
Purified anti-mouse CD48	BioLegend	BioLegend Cat# 103402; RRID: AB_313017
InVivoMab anti-mouse MHC class II (I-A)	Bio X Cell	Bio X Cell Cat# BE0178; RRID: AB_10949066
Purified anti-mouse CD107b (Mac-3)	BioLegend	BioLegend Cat# 108502; RRID: AB_313383
InVivoMab anti-mouse IL-12 p40	Bio X Cell	Bio X Cell Cat# BE0051; RRID: AB_1107698
Purified anti-mouse Ly-6A/E	BioLegend	BioLegend Cat# 108101; RRID: AB_313338
Purified anti-mouse CD88	BioLegend	BioLegend Cat# 135802; RRID: AB_1953295
Rat Anti-Ly-6G Monoclonal Antibody	BD Biosciences	BD Biosciences Cat# 551459; RRID: AB_394206
Purified anti-mouse Ly-6C	BioLegend	BioLegend Cat# 128002; RRID: AB_1134214
CD9 antibody	BD Biosciences	BD Biosciences Cat# 553758; RRID: AB_395032
Siglec-F antibody	BD Biosciences	BD Biosciences Cat# 552125; RRID: AB_394340
LEAF Purified anti-mouse Tim-4	BioLegend	BioLegend Cat# 130004; RRID: AB_1227800
Purified anti-mouse CD49b	BioLegend	BioLegend Cat# 108902; RRID: AB_313409
CD11b antibody	BD Biosciences	BD Biosciences Cat# 553308; RRID: AB_394772)
CD86 antibody	BD Biosciences	BD Biosciences Cat# 553689; RRID: AB_394991
Rat Anti-Mouse CD68 Monoclonal antibody	Bio-Rad	Bio-Rad Cat# MCA1957; RRID: AB_322219
BST2 Antibody (120G8.04)	Novus	Novus Cat# DDX0390P-100; RRID: AB_2827525
Mouse Mer Antibody	R&Dsystems	R&Dsystems; Cat# BAF591
Purified anti-mouse CD11c antibody	BioLegend	BioLegend Cat# 117302; RRID: AB_313771
Clec4F antibody	R&Dsystems	R&Dsystems; Cat# AF2784
F4/80 antibody	Bio-Rad	Bio-Rad Cat# MCA497; RRID: AB_2098196
Purified anti-mouse CD206	BioLegend	BioLegend Cat# 141702; RRID: AB_10900233
Purified anti-mouse CD43	BioLegend	BioLegend Cat# 143202; RRID: AB_11124103
CD81 antibody	BD Biosciences	BD Biosciences Cat# 559518; RRID: AB_397259

(*Continued on next page*)

Continued

REAGENT or RESOURCE	SOURCE	IDENTIFIER
CD226 (DNAM-1) Monoclonal Antibody	Thermo Fisher Scientific	Thermo Fisher Scientific Cat# 16-2261-81; RRID: AB_1724031
Purified anti-mouse CD103 antibody	BioLegend	BioLegend Cat# 121402; RRID: AB_535945
Purified anti-mouse CD64 (FcgammaRI) antibody	BioLegend	BioLegend Cat# 139302; RRID: AB_10613107
Purified anti-mouse CD169 (Siglec-1) antibody,	BioLegend	BioLegend Cat# 142402; RRID: AB_10916523
anti-CCR2 antibody	R&Dsystems	R and D Systems Cat# MAB55381-100; RRID: AB_2749828
LYVE1 Monoclonal Antibody	Thermo Fisher Scientific	Thermo Fisher Scientific Cat# 14-0443-37; RRID: AB_2864884
CD102 (ICAM-2) Monoclonal Antibody	Thermo Fisher Scientific	Thermo Fisher Scientific Cat# 16-1021-82; RRID: AB_2573077
Purified anti-mouse CD107a (LAMP-1) antibody	BioLegend	BioLegend Cat# 121602; RRID: AB_572021
Purified anti-mouse Siglec H antibody	BioLegend	BioLegend Cat# 129602; RRID: AB_1227757
CD172a antibody	BD Biosciences	BD Biosciences Cat# 552371; RRID: AB_394371
Purified anti-mouse CD24 antibody	BioLegend	BioLegend Cat# 101802; RRID: AB_312835
Purified anti-mouse CD200R (OX2R) antibody	BioLegend	BioLegend Cat# 123902; RRID: AB_1227747
InVivoMab anti-mouse Thy1 (CD90)	Bio X Cell	Bio X Cell Cat# BE0212; RRID: AB_2687698
Monoclonal Anti-HA antibody	Sigma-Aldrich	Sigma-Aldrich Cat# H9658; RRID: AB_260092
IgG1 Isotype Control	Sigma-Aldrich	Sigma-Aldrich Cat# M5284; RRID: AB_1163685
Alexa Fluor® 488 anti-mouse F4/80 antibody	BioLegend	BioLegend Cat# 123120; RRID: AB_893479
APC anti-mouse CD206 (MMR) antibody	BioLegend	BioLegend Cat# 141708; RRID: AB_10900231
Alexa Fluor® 594 anti-mouse CD38 antibody	BioLegend	BioLegend Cat# 102725; RRID: AB_2566435
Chemicals, peptides, and recombinant proteins		
Lysyl EndopeptidaseR (Lys-C)	Wako	Wako Cat# 129-02541
Collagenase type IV	Sigma	Sigma Cat #C5138
DNaseI	Thermo Fisher Scientific	Thermo Fisher Scientific Cat# EN0521
Sequencing Grade Modified Trypsin	Promega	Promega Cat# V5117
RNasin® Ribonuclease Inhibitor	Promega	Promega Cat# N2511
Cycloheximide	Sigma	Sigma Cat# 66-81-9
Dynabeads Protein G	Thermo Fisher Scientific	Thermo Fisher Scientific Cat# 10003D
O.C.T.	Killik Bio-Optica	Killik Bio-Optica Cat# 05-9801
DAPI	Sigma	Sigma Cat# 28718-90-3
FluorSave Reagent	Millipore	Millipore Cat# 34578
Critical commercial assays		
Pierce BCA Protein Assay Kit	Thermo Fisher Scientific	Thermo Fisher Scientific Cat# 23227
Amplex Red Hydrogen Peroxide/Peroxidase Assay Kit	Thermo Fisher Scientific	Thermo Fisher Scientific Cat# A22188
Lipid Peroxidation (MDA) Assay Kit (Colorimetric/ Fluorometric)	Abcam	Abcam Cat# ab118970
Arcturus PicoPure® RNA Isolation kit	Thermo Fisher Scientific	Thermo Fisher Scientific Cat# KIT0204
DNA High Sensitivity Reagent Kit	Perkin Elmer	Perkin Elmer Cat# CLS760672
Illumina Nextera XT kit	Illumina	Illumina Cat# FC-131-1024
Deposited data		
Single-cell RNaseq data	This manuscript	NCBI Gene Expression Omnibus(GEO) accession #168989. GEO:168989.
Experimental models: Organisms/strains		
Mouse: C57BL/6	The Jackson Laboratory	C57BL/6 colony
Oligonucleotides		
5′-GCAAAUGCAAAGAAGGAAA-3′	Dharmacon	N/A
5′-CAGUCGCGUUUGCGACUGG-3′	Dharmacon	N/A

(*Continued on next page*)

Continued

REAGENT or RESOURCE	SOURCE	IDENTIFIER
Software and algorithms		
FlowJo V10	FlowJo	https://www.flowjo.com/
R v4.4	The R Foundation	https://www.r-project.org
CytofKit	Chen et al., 2016	https://bioconductor.riken.jp/packages/3.3/bioc/html/cytofkit.html
Seurat v2	Butler et al., 2018	https://satijalab.org/seurat/
Seurat v3	Stuart et al., 2019	https://satijalab.org/seurat/
One sense	Cheng et al., 2016	N/A
MaxQuant 1.6.7.0	MaxQuant	https://www.maxquant.org
Subread package	N/A	http://subread.sourceforge.net
edgeR	Robinson et al., 2010	http://bioconductor.org/packages/release/bioc/html/edgeR.html
LIMMA R package	Ritchie et al., 2015	https://bioconductor.org/packages/release/bioc/html/limma.html
COMBAT	Wang et al., 2017	https://cran.r-project.org/web/packages/COMBAT/index.html
Short Time-series Expression Miner (STEM)	N/A	https://www.cs.cmu.edu/~jernst/stem/
Imaris bitplane	Imaris	https://imaris.oxinst.com/products/imaris-for-cell-biologists?gclid=Cj0KCQiAgomBBhDXARIsAFNyUqOQMD64vZvZMyBoHWFOYRm_ZPxHWLb_tWDl0pGjii8ZVNDkW-UNtRgaAnhfEALw_wcB
Other		
LSRII	BD Biosciences	N/A
Imagestream Amnis	Merk	N/A
FACSAria II	BD Bioscience	N/A
FACSAria III	BD Bioscience	N/A
Mindray BS-240 Pro	BioSentec	N/A
Easy LC 1000	Thermo Scientific	N/A
Obritrap Fusion Lumos	Thermo Scientific	N/A
Agilent Bioanalyser	Agilent	N/A
Perkin Elmer Labchip	Perkin Elmer	N/A
Illumina HiSeq 4000 system	Illumina	N/A
Chromium Single Cell 3′ (v3 Chemistry)	10x Genomics	N/A
SP5 confocal microscope	Leica Microsystem	N/A
JSM-6701F scanning electron microscope	JEOL Ltd.	N/A

RESOURCE AVAILABILITY

Lead contact

Further information and requests for resources and reagents should be directed to and will be fulfilled by the lead contact Florent Ginhoux, Florent_Ginhoux@immunol.a-star.edu.sg.

Materials availability

This study did not generate new unique reagents.

Data and code availability

Single-cell RNA-seq data have been deposited at GEO and are publicly available as of the date of publication. Accession numbers are listed in the key resources table. Any additional information required to reanalyze the data reported in this paper is available from the lead contact upon request.

METHOD DETAILS

Animal models

Mice

All mouse experiments and procedures were approved by the Institutional Animal Care and Use Committee of the Biological Resource Center (Agency for Science, Technology and Research, Singapore) in accordance with the guidelines of the Agri-Food and Veterinary Authority and the National Advisory Committee for Laboratory Animal Research of Singapore (ICUAC No. 181402). The C57/BL6 mice were obtained from the Jackson Laboratory. All mice were bred and housed in the Biological Resource Centre animal facility under Specific Pathogen-Free conditions and are maintained on a C57BL/6 background. All mice used in the *in vivo* experiments were aged 7 to 12 weeks unless specified. Mice were given high fat diet (60% fat - #D12492 Research Diets Inc.) *ab libitum* or tamoxifen-enriched diet (Teklad TD.130855 EnVigo) when specified. For the glucose tolerance test, mice were fasted overnight and then received 2 $g.kg^{-1}$ of glucose by oral gavage according to Andrikopoulos et al. (2008). Glycaemia was then measured at indicated time points.

Indirect calorimetric measurement (metabolic chamber)

For the metabolic cage study, mice were housed individually in metabolic chambers and maintained on a 12-hr dark-light cycle with lights from 6am to 6pm at 22°C. Oxygen consumption, CO_2 emission, food consumption, movement and energy expenditure were measured using TSA metabolic chambers (TSA System, Germany) in an open-circuit indirect calorimetric system.

GERPs administration

GERPs were prepared as previously described (Tesz et al., 2011). Mice fed with HFD for 8 weeks were first randomized according to their body weight and glucose tolerance. Then mice were treated with a total dose of 2mg GERPs loaded with siRNA against Cd36 (5′-GCAAAUGCAAAGAAGGAAA-3′) or with negative control (Scr: 5′-CAGUCGCGUUUGCGACUGG-3′) (Dharmacon) (80μg), and Endoporter (0,1mM). Mice received six doses of fluorescently labeled (FITC) GERPs by i.v injections over 15 days.

Mouse biochemical parameters

Liver samples were collected and immediately flash frozen. From these, total triglyceride (TG) content was determined by a commercially available colorimetric kit (Roche; TG 12016648). TG concentration was normalized against protein concentration as determined by the Pierce BCA protein assay kit (Thermofisher;23227) following the manufacturer's instructions. Intracellular amount of H2O2 was measured using Amplex Red Hydrogen Peroxide/Peroxidase Assay Kit (Life Technologies; A22188). Malondialdehyde content was measured using a Lipid Peroxidation (MDA) Assay Kit (Colorimetric/Fluorometric) (Abcam; ab118970). Plasma multi-analyte profiling was performed using a clinical chemistry analyzer (Mindray BS-240 Pro, BioSentec) with the indicated colorimetric kits (all from Biosentec). All assays were performed following manufacturer's instructions.

Cell preparation

Cell isolation, flow cytometry and sorting of macrophages

Standard labeling procedures were used to prepare the cells for flow cytometry analysis. Hepatocytes were isolated by centrifugation using a density gradient as previously described (Aparicio-Vergara et al., 2017). For macrophages, liver lobules were digested in collagenase/DNase I (0.2 $mg.ml^{-1}$ of collagenase, 5 $units.ml^{-1}$ of DNase I and 10% FBS in RPMI) for 30 minutes at 37°C and dissociation was finalised by several passages through a needle 18G. No enrichment was performed to avoid any cell loss and isolated cells were directly stained for flow cytometry after red blood cell lysis. The antibodies used are listed in the key resources table. Data were acquired by LSRII (BD Bioscience) or Imagestream Amnis (Merck) and analyzed by Flow Jo (Tree Star, Inc.). Cells were sorted using a FACS Aria II or III (BD Bioscience).

CyTOF

Cells were prepared, labeled and data recorded as previously described (Blériot et al., 2020b). Briefly, cells were prepared as for conventional flow cytometry and stained with cisplatin to determine cell viability. Antibodies used are listed in Table S2. Results were analyzed using CytofKit (Chen et al., 2016) and One-sense algorithms (Cheng et al., 2016).

Mass spectrometry

Sorted cell populations were lysed in Urea lysis buffer (8M Urea /Tris-HCl 50mM, pH 8), reduced in presence of TCEP 20mM for 20 min at room temperature and further alkylated with 55mM chloroacetamide. Following dilution with 100mM triethylammonium bicarbonate (TEAB, pH8.5; Sigma-Aldrich #T7408) samples were digested with Lysyl endopeptidase (LysC, Wako #129-02541) and Trypsin (Promega, #V5117) in ratio (1:100) for 4h and 18h respectively. Samples were further acidified with trifluoroacetic acid (TFA Sigma-Aldrich #T6508; 1% v/v) spun down 14,000 RPM for 10min at room temperature and desalted using HLB 96 well plate (Waters, #WAT058951). Following crude step high pH reverse phase fractionation (4 fractions, Reposil-Pur Basic C18 10μm, Dr Maisch Gmbh #r10.b9.0025). Each fraction was separated on a 50cm (id 75μm) EASY-Spray RP-C18 LC column (Thermo Scientific) in a 75 minutes gradient of solvent A (0.1% Formic acid in water) and solvent B (99.9% acetonitrile, 0.1% Formic acid in water) on Easy LC 1000 (Thermo Fisher Scientific), coupled to Obritrap Fusion Lumos mass spetrometer (Thermo Fisher Scientific). Peak lists were generated using MaxQuant software version 1.6.7.0. Spectra were searched against target-decoy Mouse Uniprot database with following fixed modifications: Carbamidomethyl (C) and variable modifications: Oxidated (M), Deamidated (NQ) Acetyl (N-terminal protein). Maximum 2 missed cleavages were allowed, mass tolerance: 4.5 ppm mass deviation (after recalibration) for OT-MS survey scan and 0.5 Da for IT-MS/MS ion fragments. FDR was set to 1%. Label free LFQ quantitation was performed.

Transcriptomics

Library preparation

For bulk RNaseq experiments, between 20,000 and 50,000 cells were FACS-sorted and total RNA was extracted using Arcturus PicoPure® RNA Isolation kit (Arcturus® Thermo Fisher Scientific, Waltham, MA, USA) according to manufacturer's protocol. All Mouse RNAs were analyzed on Agilent Bioanalyser (Agilent, Santa Clara, CA, USA) for quality assessment with RNA Integrity Number (RIN) range from 5.8 to 6.7 and median of RIN 6.4. cDNA libraries were prepared using 2 ng of total RNA and 1ul of a 1:50,000 dilution of ERCC RNA Spike in Controls (Ambion® Thermo Fisher Scientific, Waltham, MA, USA) using the Smart-Seq v2 protocol (Picelli et al., 2014) with the following modifications: 1. Addition of 20 μM TSO; 2. Use of 200 pg cDNA with 1/5 reaction of Illumina Nextera XT kit (Illumina, San Diego, CA, USA). The length distribution of the cDNA libraries was monitored using a DNA High Sensitivity Reagent Kit on the Perkin Elmer Labchip (Perkin Elmer, Waltham, MA, USA). All samples were subjected to an indexed paired-end sequencing run of 2x151 cycles on an Illumina HiSeq 4000 system (Illumina) (25 samples/lane).

For Smart-seq2 single cell analysis, 288 single cells were sorted on a 96-well plate and cDNA libraries were generated using the Smart-seq v2 protocol (Picelli et al., 2014) with the following modifications: 1. 1mg/ml BSA Lysis buffer (Ambion® Thermo Fisher Scientific, Waltham, MA, USA); 2. Use of 200 pg cDNA with 1/5 reaction of Illumina Nextera XT kit (Illumina, San Diego, CA, USA). The length distribution of the cDNA libraries was monitored using a DNA High Sensitivity Reagent Kit on the Perkin Elmer Labchip (Perkin Elmer, Waltham, MA, USA). All samples were subjected to an indexed paired-end sequencing run of 2x151 cycles on an Illumina HiSeq 4000 system (Illumina, San Diego, CA, USA) (298 samples/lane). After QC filtering, 169 cells were used for analysis.

For 10X analysis, samples were processed using the Chromium Single Cell 3′ (v3 Chemistry) platform (10x Genomics, Pleasanton, CA). Briefly, 100,000 cells $CD45^+$ $Tomato^-$ including the KC and 100,000 cells $CD45^+$ $Tomato^+$ were pooled and sequenced on Novaseq lanes by Novagene AIT. After QC filtering, 78,944 cells were used for analysis.

For RiboTag analysis, samples were prepared as described elsewhere (Haimon et al., 2018). Briefly, 50,000 cells were sorted and resuspended on ice in 1ml of lysis buffer (50 mM Tris, pH 7.4, 100 mM KCl, 12 mM MgCl2, 1% NP-40, 1 mM DTT, 1:100 protease inhibitor (Sigma Aldrich), 200 units/ml RNasin (Promega) and 0.1 mg/ml cycloheximide (Sigma Aldrich) in RNase free water). To remove cell debris, homogenate was transferred to an Eppendorf tube and was centrifuged at 10,000 g and 4°C for 10 min. Supernatants were transferred to a fresh Eppendorf tube on ice and 5 μL (= 125 μg) of anti-HA antibody (H9658, Sigma Aldrich) or 5 μL (= 1 μg) of mouse monoclonal IgG1 antibody (Sigma, Cat# M5284) was added to the supernatant, followed by 4 h of incubation with slow rotation in a cold room at 4°C. Meanwhile, Dynabeads Protein G (Thermo Fisher Scientific), 100 μL per sample, were equilibrated to homogenization buffer by washing three times. At the end of 4 h of incubation with antibodies, beads were added to each sample, followed by incubation overnight in cold room at 4°C. Samples were washed three times with high-salt buffer (50 mM Tris, 300 mM KCl, 12 mM MgCl2, 1% NP-40, 1 mM DTT, 1:200 protease inhibitor, 100 units/ml RNasin and 0.1 mg/ml cycloheximide in RNase free water), 5 min per wash in a cold room on a rotator. At the end of the washes, beads were magnetized and excess buffer was removed. Purified RNA was then treated as the single cell samples, considering the low amount of RNA harvested. cDNA libraries were generated using the above single cell RNA sequencing method except the use of 300pg cDNA for Illumina Nextera XT kit.

For the Rhapsody experiment, all the process was done by following manufacturer's (BD Biosciences) protocol. 16,775 cells were captured in a single run with 12 barcoded samples pooled together. The sample was processed according to BD mRNA targeted and sample tag library preparation with the BD Rhapsody™ targeted mRNA and Abseq amplification kit (Doc ID: 210969 Rev 3.0). Samples were then subjected to an indexed paired-end sequencing run of 2x151 cycles on an Illumina HiSeq 4000 system (Illumina, San Diego, CA, USA) with 20% PhiX spike in.

Analysis of transcriptomic data

Raw reads were aligned to the mouse reference genome GRCm38_M13 from GENCODE using STAR 2.5.3a (Dobin et al., 2013). Gene expression values in transcripts per million (TPM) were calculated using the same RSEM program (Li and Dewey, 2011). Dimensionality reduction (PCA, tSNE and UMAP), clustering and differentially expressed genes (DEGs) analysis were conducted using Seurat version 2.4.3 (Butler et al., 2018). Wilcoxon rank sum test was performed to calculate differentially expressed genes p value. After got the p value, p value adjustment was performed using Bonferroni correction based on the total number of genes in the dataset and adjusted p value < 0.05 was used as a threshold for statistical significance. 10X and SMARTSeq2 data integration was conducted using Seurat version 3.0.1 (Stuart et al., 2019) with standard integration pipeline.

Imaging

Confocal imaging

KC1 and KC2 were labeled for confocal immunofluorescence imaging by i.v. injection of 2 μg F4/80 Alexa flour 488 (Biolegend #123120) and 2 μg CD206-APC (Biolegend #141708) into WT C57BL/6 mice 10 min prior to sacrifice of the animal. Liver lobes were fixed overnight in PBS with 4% paraformaldehyde, then incubated for 24h in PBS with 30% sucrose. Subsequently liver lobes were either embedded into O.C.T (Killik Bio-Optica #05-9801) and cut into 60 μm thick sections with a cryostat at −14°C or embedded in 4% low-melting-point agarose (Sigma-Aldrich) for 200 μM thick vibratome sections. For O.C.T-embedded tissues, sections were blocked for 15 min with blocking buffer (PBS, 0.5% BSA, 0.3% Triton), then stained for 60 min at RT with CD38 Alexa flour 594 (Biolegend #102725) in wash/stain buffer (PBS, 0.2% BSA, 0.1% triton), washed twice for 5 min, stained with DAPI (Sigma #28718-90-3**)** for 5 min, washed again and mounted for imaging with Fluorosave™ Reagent (Millipore #345789). Images were acquired with an SP5 confocal microscope (Leica) with an 63x oil-immersion objective. For visualization purposes and to compensate for uneven slide illumination, layer fluorescent intensity was normalized using Imaris Normalize Layers tool.

Subsequently autofluorescence was filtered from the image by channel subtraction of a deep red autofluorescent channel from APC signal with Imaris Channel Arithmetics tool. For agarose-embedded tissues, sections were permeabilized for 1 h in PBS supplemented with 0.4% Triton X-100 (Sigma-Aldrich) and 3% BSA (Sigma-Aldrich) and preincubated for 1 h in the blocking buffer (PBS supplemented with 3% BSA). Then tissues were labeled with the appropriate primary and secondary antibodies for 2 h at room temperature.

Scanning electron microscopy

Cells were fixed in 2.5% glutaraldehyde in 0.1 M phosphate buffer for 1 hr (pH 7.4) at room temperature, treated with 1% osmium tetroxide (Ted Pella Inc) at room temperature for 1 hr, and then dehydrated through a graded ethanol series from 25% to 100% and dried using a CPD 030 critical point dryer (Bal-Tec AG, Liechtenstein). The surface on which the cells were grown and the adhesive surface was coated with 5 nm of gold by sputter coating using a SCD005 high-vacuum sputter coater (Bal-Tec AG). The coated samples were examined with a field emission JSM-6701F scanning electron microscope (JEOL Ltd., United States) at an acceleration voltage of 8 kV using the in-lens secondary electron detector.

QUANTIFICATION AND STATISTICAL ANALYSIS

DEG analyses were performed using the Seurat v3 package (Stuart et al., 2019). All DEGs obtained from tpm/count matrixes were calculated on normalized values with a logFC threshold of 0.25. Wilcoxon rank sum test was performed to calculate differentially expressed genes p value. After got the p value, p value adjustment was performed using Bonferroni correction based on the total number of genes in the dataset and adjusted p value < 0.05 was used as a threshold for statistical significance.